Measurement Report: Characterization of Aerosol Hygroscopicity over Southeast Asia during the NASA CAMP²Ex Campaign

Genevieve Rose Lorenzo[1,2], Luke D. Ziemba[3], Avelino F. Arellano[1], Mary C. Barth[4], Ewan C. Crosbie[3,5], Joshua P. DiGangi[3], Glenn S. Diskin[3], Richard Ferrare[3], Miguel Ricardo A. Hilario[1], Michael A. Shook[3], Simone Tilmes[4], Jian Wang[6], Qian Xiao[6], Jun Zhang[4], and Armin Sorooshian[1,7]

[1]Department of Hydrology and Atmospheric Sciences, University of Arizona, Tucson, Arizona, 85721, USA
[2]Manila Observatory, Quezon City, 1108, Philippines
[3]NASA Langley Research Center, Hampton, Virginia, 23681 USA
[4]Atmospheric Chemistry Observations & Modeling Laboratory, NSF National Center for Atmospheric Research, Boulder, Colorado, 80301, USA
[5]Analytical Mechanics Associates, Inc, Hampton, Virginia, 23666 USA
[6]Department of Energy, Environmental & Chemical Engineering, Washington University in St Louis, St. Louis, Missouri, 63130, USA
[7]Department of Chemical and Environmental Engineering, University of Arizona, Tucson, Arizona, 85721, USA

Correspondence to: armin@arizona.edu

Abstract. This study characterizes the spatial and vertical nature of aerosol hygroscopicity in Southeast Asia and relates it to aerosol composition and sources. Aerosol hygroscopicity via the light scattering hygroscopic growth factor, $f(RH)$, is calculated from the amplification of PM_5 aerosol ($D_p < 5$ μm) scattering measurements from < 40 % to 82 % relative humidity during the Cloud, Aerosol, and Monsoon Processes Philippines Experiment (CAMP²Ex) between August to October 2019 over the northwest tropical Pacific. Median $f(RH)$ is low (1.26 with lower to upper quartiles of 1.05 to 1.43) like polluted environments, due to the dominance of the mixture of organic carbon and elemental carbon. The $f(RH)$ is lowest due to smoke from the Maritime Continent (MC) during its peak biomass burning season, coincident with high carbon monoxide concentrations (> 0.25 ppm) and pronounced levels of accumulation mode particles and organic mass fractions. The highest $f(RH)$ values are linked to coarser particles from the West Pacific and aged biomass burning particles in the region farthest away from the MC, where $f(RH)$ values are lower than typical polluted marine environments. Convective transport and associated cloud processing in these regions decrease and increase hygroscopicity aloft in cases with transported air masses exhibiting increased organic and sulfate mass fractions, respectively. An evaluation of a global chemical transport model (CAM-chem) for cases of vertical transport showed the underrepresentation of organics resulting in overestimated modeled aerosol hygroscopicity. These findings on aerosol hygroscopicity can help to improve aerosol representation in models and the understanding of cloud formation.

1. Introduction

Aerosol particles affect climate and visibility through the direct and indirect extinction of solar radiation via absorption and scattering of light and through cloud formation, respectively. Aerosol hygroscopicity compounds aerosol effects on Earth's radiation budget (Zhao et al., 2018; Malm and Day, 2001), secondary aerosol formation and cloud formation (Köhler, 1936), and health (Dockery, 2001). Neglecting the effect of moisture on aerosol growth leads to incorrect estimation of the cooling at Earth's surface due to aerosol particles (Garland et al., 2007). For instance, a decrease in light extinction over the southeast U.S. was linked to reduced aerosol water uptake, coincident with decreases in the sulfate/organic ratio (Attwood et al., 2014). Particle aging/coating can cause underestimation of both aerosol hygroscopicity in the sub-saturated regime (Wang et al., 2018) and cloud condensation nuclei (CCN) activity in the supersaturated regime for aged particles in China by ~22 % (Zhang et al., 2017). Remote sensing of aerosol optical properties is also affected by aerosol water content (Ferrare et al., 1998; Ferrare et al., 2023). Therefore, accurate aerosol hygroscopicity values are critical for remote sensing and satellite observation of aerosol particles (Ziemba et al., 2013; van Diedenhoven et al., 2022).

Aerosol hygroscopicity is described by physical quantities such as the diameter growth factor, g(RH), and light scattering hygroscopic growth factor, f(RH). The g(RH) parameter relates the wet particle diameter of the aerosol at a high relative humidity to the dry diameter of the aerosol at low relative humidity, while f(RH) relates total scattering due to the aerosol at high relative humidity (80 %) to that at low relative humidity (<40 %) (Waggoner et al., 1983; Hegg et al., 1993). Light scattering increases with relative humidity for most particles and is correlated to chemical composition and size (Baynard et al., 2006; Swietlicki et al., 2008) of particulate matter (Covert et al., 1972; Brock et al., 2016a).

Direct measurement of aerosol hygroscopicity, however, is difficult and is also not well-represented in climate models (Chen et al., 2014). The hygroscopicity parameter kappa, κ, is a single parameter that was developed to represent water uptake in models. It determines the volume (or mass or moles, with appropriate unit conversions) of water that is associated with a unit volume of a dry aerosol particle (Petters and Kreidenweis, 2007). A simple and commonly used water uptake model for calculating kappa is based on the Zdanovskii, Stokes, and Robinson (ZSR) treatment for water soluble organic-inorganic mixed aerosol particles (Stokes and Robinson, 1966) where it is assumed that there are no interactions between the organic and inorganic species. In the ZSR model, water uptake of the individual non-interacting components can be summed up linearly to represent the total water uptake of the mixed aerosol. The interaction of organics and inorganics, however, along with the aging-specific density of organics is thought to influence hygroscopicity and affect both the ZSR calculation (Fan et al., 2020) and aerosol particle growth factor via changes in molecular structure, molecular weight, functionality, and/or other properties (Swietlicki et al., 2008).

67   Observed and simulated aerosol hygroscopicity are greater in clean marine air masses (f(RH=85 %/RH=40 %) = 2.10

68   - 2.30 for PM_1) compared to air masses over land and near terrestrial biogenic sources (f(RH=85 %/RH=40 %) = 1.29

69   - 2.10 for PM_1), which are secondary organics precursors, and from biomass burning (f(RH=85 %/RH=40 %) = 1.02

70   – 2.10 for PM_1) (Swietlicki et al., 2008; Duplissy et al., 2011; Petters and Kreidenweis, 2007; Burgos et al., 2019;

71   Titos et al., 2021; Gomez et al., 2018). Only the Arctic has aerosol hygroscopicity (f(RH=85 %/RH=40 %) = 2.70 for

72   PM_1 and f(RH=85 %/RH=40 %) = 3.00 for whole-air samples) values greater than in clean marine regions (Delene

73   and Ogren, 2002; Zieger et al., 2010). In marine areas, hygroscopicity typically decreases with altitude with decreasing

74   inorganic fractions (Pringle et al., 2010). Cloud processing over marine areas has been observed to increase the

75   oxidation of organic aerosols (Che et al., 2022; Dadashazar et al., 2022) and hygroscopicity in general (Crumeyrolle

76   et al., 2008). Continental aerosol particles have smaller diameters and are usually less hygroscopic due to more

77   organic-rich aerosol particles (κ = 0 - 0.1 from Table S1) and pure elemental carbon particles (EC, κ = 0 - 0.035 from

78   Table S1) (Wang et al., 2014; Kreidenweis and Asa-Awuku, 2014). Organics are generally less hygroscopic than

79   inorganics (κ = 0.56 – 1.24 from Table S1), and their hygroscopicity is affected by oxidation level (e.g., O:C ratio),

80   oxidation state, and solubility (Brock et al., 2016a; Wu et al., 2016; Thalman et al., 2017). Aging has also been found

81   to increase aerosol hygroscopicity through the oxidation of secondary organic aerosols and organic aerosol interactions

82   with inorganics (Engelhart et al., 2008; Liu et al., 2014; Saxena et al., 1995).

83   Although aerosol studies in the rapidly developing Southeast Asia (SEA) region are increasing, few are focused on

84   the nature of aerosol particles and their interactions with water vapor and clouds (Tsay et al., 2013; Ross et al., 2018;

85   Reid et al., 2023). There has been no comprehensive study of aerosol hygroscopicity in and around the Philippines in

86   Southeast Asia. Understanding the interactions between aerosols and the complex geographic, meteorological, and

87   hydrological environment in Southeast Asia remains challenging due to a still growing observational database,

88   prevalence of clouds interfering with remote sensing, and limited modeling studies (Tsay et al., 2013; Lee et al., 2018;

89   Chen et al., 2020; Hong and Di Girolamo, 2020; Amnuaylojaroen, 2023). This, along with increased local and

90   transported emissions and prevalent moisture-rich conditions in the region, altogether motivate the need to understand

91   aerosol hygroscopicity and associated impacts on radiative transfer and on climate (Brock et al., 2016a; Ziemba et al.,

92   2013). How freshly emitted nearly hydrophobic particles transform into hygroscopic aerosol particles (Swietlicki et

93   al., 2008), for example, is an understudied topic in Southeast Asia where there are significant sources of particles

94   with low hygroscopicity (Reid et al., 2023). Understanding aerosol hygroscopicity will also help in the need to improve

95   remote sensing measurements in the region, which is affected by overlapping high and low level clouds (Burgos et

96   al., 2019; Hong and Di Girolamo, 2020).

97   Predicting aerosol hygroscopicity, especially at higher relative humidity (RH), is especially difficult due to optical

98   instruments underestimating particle light scattering at high RH and mechanisms other than hygroscopicity impacting

99   particle growth (Gasparini et al., 2006; Mochida et al., 2006). This is important because atmospheric water content is

100 high in Southeast Asia. For example, the hygroscopicity of secondarily formed organics (via gas-to-particle

101 conversion) is found to be dependent on oxidation state for high RH (Shi et al., 2022). Southeast Asia has elevated

102   levels of organics, inorganics, and elemental carbon (Cruz et al., 2019; AzadiAghdam et al., 2019; Oanh et al., 2006),
103   allowing for an opportunity to see how hygroscopicity responds to a range of relative values of each of these elevated
104   components. Therefore, relating aerosol particle composition to hygroscopicity, for closure (Xu et al., 2020), is
105   particularly significant there.

106   Aerosol hygroscopicity is a crucial factor in the understanding and modeling of aerosol-cloud interactions, because of
107   the role hygroscopicity plays in cloud drop activation. The NASA Cloud, Aerosol, and Monsoon Processes Philippines
108   Experiment (CAMP^{2}Ex) was designed to understand the role of aerosol particles in cloud formation and in regulating
109   solar radiation during the southwest monsoon (Reid et al., 2023). CAMP^{2}Ex occurred between August and October
110   2019 over the Philippines and neighboring areas. The campaign provides an aircraft dataset with measurements
111   focused on aerosol and cloud properties, which affords a valuable opportunity to evaluate models with these
112   measurements for shallow to moderate convection, which is one of the biggest challenges for regional and global-
113   scale atmosphere models to represent because these clouds are much smaller than the model grid spacing.

114   Global atmospheric model evaluation of aerosol extinction for the CAMP^{2}Ex region suggests that biomass burning
115   aerosol hygroscopicity is over-estimated by global atmosphere models, with both the model size representation of the
116   aerosol particles and the size discrepancy between model and observations contributing to this (Collow et al., 2022;
117   Edwards et al., 2022). The findings from Collow et al. (2022) and Edwards et al. (2022) bring up the need for a more
118   thorough understanding of the components of biomass burning aerosols in the region that affect observed and modeled
119   hygroscopicity. The overestimation of hygroscopicity due to biomass burning can affect the representation of clouds
120   in the region. Clouds, especially shallow cumulus clouds, like those in the tropical West Pacific (which the CAMP^{2}Ex
121   region is part of) have been underestimated by models due to the lack of observational data to improve convective
122   parameterizations (Chandra et al., 2015). Part of the challenge in modeling aerosol-cloud interactions is the ability to
123   both have a high-resolution representation, at the scale of the shallow convection, in a large enough domain, which is
124   important for understanding climatic effects to properly account for the bulk behavior of cloud fields (Spill et al.,
125   2019). This could be addressed by evolving modeling infrastructures, with higher resolution schemes ranging from
126   regional to convective scale within a larger domain (Pfister et al., 2020; Radtke et al., 2021).

127   Knowledge gaps identified above are addressed in this study using the CAMP^{2}Ex dataset. To our knowledge, this is
128   the first time this dataset has been explored extensively to characterize aerosol hygroscopicity properties in the region.
129   The goals of this proposed study are to (i) characterize the spatial distribution of aerosol hygroscopicity in Southeast
130   Asia during the CAMP^{2}Ex airborne mission, (ii) relate aerosol hygroscopicity and composition, (iii) identify emission
131   events that impact aerosol hygroscopic growth, and (iv) evaluate a global chemical transport model with regional
132   refinement for aerosol vertical transport.
133
134   **2. Methods**

135   **2.1 CAMP^{2}Ex Field Campaign**

136 CAMP^{2}Ex included 19 research flights with a NASA P3 from 24 August to 5 October 2019. Twelve of these flights
137 were associated with the southwest monsoon (SWM) followed by a flow reversal with seven flights conducted during
138 the northeast monsoon (NEM) (Reid et al., 2023). As summarized by Reid et al. (2023), the combination of airborne
139 and ship-based measurements helps to characterize interactions between various aerosol particle sources (e.g., biomass
140 burning, industrial, natural) and small to congestus convection. Below we note the P3 instruments most relevant to
141 this study.

142 **2.2 Observations and Derived Quantities**

143 **2.2.1 P3 Instrumentation**

144 As summarized in Table 1, data are used from a variety of aerosol particle and trace gas instrumentation. The aerosol
145 particle scattering and absorption instruments measure the optical properties of bulk aerosol particles (PM$_5$): < 5 μm
146 dry diameter (McNaughton et al., 2007). Aerosol composition and size data for submicrometer particles were
147 considered when they were collected using a forward-facing shrouded isokinetic inlet. Non-refractory species in the
148 submicrometer range studied using an aerosol mass spectrometer (AMS) included sulfate, nitrate, ammonium,
149 organics, and chloride. We also use the ratio of the mass spectral marker m/z 44 marker relative to total organic mass,
150 f_{44}, as a possible indicator of air mass age. Submicrometer refractory species of black carbon (also referred to as
151 elemental carbon) from a single particle poot photometer (SP2) were also included in the study. Bulk water-soluble
152 aerosol particles were collected using a particle-into-liquid sampler (PILS) and were analyzed using ion
153 chromatography; species quantified included oxalate, NH_4^+, dimethylamine (DMA), K^+, SO_4^{2-}, Ca^{2+}, Na^+, Mg^{2+}, Cl^-,
154 NO_3^-, Br^-, and NO^-. Cloud-free conditions are identified to ensure the highest quality aerosol data using a cloud flag
155 product based on measurements from the fast cloud droplet probe (FCDP) and two-dimensional stereo probe (2D-S).
156 Aerosol particle composition data are considered for those cases when the total aerosol non-refractory particle mass
157 was greater than 0.4 μg sm^{-3}.

158 **Table 1: Summary of instrument data used in this work.**

Parameter	Instrument	Time Resolution	Uncertainty	Sampled Aerosol Particle Size	Reference
Latitude, Longitude, and Altitude	Northrop Grumman Litton 251 EGI	1 s	~5 m spherical error probable; 0.01°	N/A	Reid et al., 2023
Dry (RH < 40 %) and humidified (RH = 80 %)) light scattering coefficient (λ = 450, 550, 700 nm)	Parallel humidified TSI 3563 Nephelometers	1 s	30 %	< 5 μm diameter	Ziemba et al., 2013; McNaughton et al., 2007
Dry (RH < 40 %) light absorption coefficient (λ = 470, 532, 660 nm)	Radiance Research 3 Particle Soot Absorption Photometer (PSAP)	1 s	15 %	< 5 μm diameter	Mason et al., 2018; McNaughton et al., 2007
Non-refractory aerosol (Organics, SO_4, NO_3, NH_4, Cl) mass concentration	Aerodyne High-Resolution Time-of-Flight Mass Spectrometer (AMS)	25 s	LLOD (μg sm^{-3}): Organics, 0.169; SO_4, 0.039; NO_3, 0.035; NH_4, 0.169; Cl, 0.036; Uncertainty: 50 %	approximate relevant size range is 60-600 nm vac. aero. diameter	DeCarlo et al., 2008
Water-soluble mass concentration	Particle-into-liquid sampler (PILS) followed by offline ion chromatography analysis	238 s	30 %	< 5μm diameter	Sorooshian et al., 2006 Crosbie et al., 2020
Refractory black carbon (BC) mass concentration	Single Particle Soot Photometer (DMT SP2)	1 s	10 %	100 - 700 nm diameter	Schwarz et al., 2006
CO concentration	Picarro G2401-m	1 s	5 ppb	N/A	DiGangi et al., 2021
Volume and number concentration of particles	TSI Laser Aerosol Spectrometer (LAS) Model 3340	1 s	20 %	0.1 - 5 μm optical diameter	Moore et al., 2021
Volume size distribution	Fast integrated mobility spectrometer (FIMS)	1 s	Concentration: 15 %; Size: 3 %	10 – 500 nm mobility diameter	Kulkarni and Wang, 2006;

Cloud particles (data used for cloud screening)	SPEC-Hawkeye FCDP	1 s	50 %	2 – 50 μm diameter	Knollenberg 1981, Lawson et al. 2017; Woods et al. 2018
Cloud particles (data used for cloud screening)	SPEC-Hawkeye 2D-S	1 s	20 %	10 μm – 3 mm diameter	Lawson et al. 2006a, Woods et al. 2018

159

2.2.2 Aerosol Hygroscopicity, f(RH), and Other Aerosol Optical Properties

161 Aerosol hygroscopicity is reported using the parameter f(RH), which is unitless and is the amplification factor in
162 scattering due to a change in RH. The f(RH) parameter is calculated from the empirically derived exponential fit
163 coefficient gamma (γ) (Ziemba et al., 2013). The gamma parameter is based on parallel nephelometer measurements
164 of scattering at 550 nm at two different relative humidity levels: dry (< 40 %: RH_{dry}) and humidified (controlled to 82
165 ± 10 %: RH_{wet}). Gamma (Eq. 1) was calculated for times when the dry (SC_{dry}) and humidified (SC_{wet}) scattering
166 coefficients (Table 1) are greater than or equal to 5 Mm^{-1}. The f(RH) (Eq. 2) was then derived from γ (Hänel, 1976).

167

$$\gamma = \frac{\ln\frac{SC_{wet}}{SC_{dry}}}{\ln\frac{100-RH_{dry}}{100-RH_{wet}}} \qquad (1)$$

$$f(RH) = (\frac{100-RH_{wet}}{100-RH_{dry}})^{-\gamma} \qquad (2)$$

170 Each nephelometer was calibrated with pure CO_2 prior to the campaign and zero checks were performed periodically
171 during the flights to prevent baseline drift. All nephelometer scattering coefficient measurements were corrected for
172 truncation errors using a documented method (Anderson and Ogren, 1998). System response was verified in flight by
173 introducing hydrophobic PSL spheres into the sample stream to ensure that the nephelometers were consistent and an
174 f(RH) value of 1.0 is observed. Relative humidity measurements for the calculation of f(RH) were calibrated in the
175 laboratory using nebulized monodisperse 200 nm ammonium sulfate to ensure deliquescence at ~80 % RH and at the
176 typical measurement flow rates (i.e. 10 L min^{-1}) (Brooks et al., 2002). The RH was slowly ramped up from ~60 % –
177 90 % and the apparent deliquescence RH was calculated based on the sharp increase in scattering in the humidogram.
178 The offset between the calculated RH and the deliquescence RH for ammonium sulfate (i.e., ~79.5 %) was applied to
179 the data post-processing. Calibration at ~80 % RH increases the confidence in the humidified nephelometer data
180 accuracy. Non-linearities can occur at low RH measurements and add to uncertainties, but the f(RH) calculation is
181 much less sensitive at the dry end of the spectrum. Internal RH sensors were used because their placement is most
182 relevant to the sampling condition inside the nephelometer. Note that sampling efficiency decreases for

183   supermicrometer diameter particles with increasing size up to the 5-μm inlet cutoff, due to losses in transport tubing

184   and in the drying/humidification control system. Thus, derived f(RH) is applicable to accumulation-mode particles

185   and is partially sensitive to coarse-mode particles from 1-5 μm diameter.

186

187   Single scattering albedo (SSA) was calculated when both the scattering and absorption coefficients (smoothed with

188   30 s running average) were greater than 2 Mm^{-1}. The Ångström exponent (AE) was calculated using the smoothed 30

189   s running average of the scattering and absorption coefficients. The scattering Ångström exponent (SAE, 450-700

190   nm) was computed when the scattering coefficient was greater than 2 Mm^{-1} based on Ziemba et al. (2013) and the

191   absorption Ångström exponent (AAE, 470-660 nm) was computed when the absorption coefficient was greater than

192   2 Mm^{-1} to try to minimize noise issues (Mason et al., 2018). Absorption measurements were corrected for a variety of

193   errors using the method from Virkkula (Virkkula, 2010). The PSAP filters were changed before transmission dropped

194   below 70 %. This standard practice minimizes non-linearity effects due to filter loading.

195

196   **2.2.3 Sea Salt**

197   Bulk sea salt mass concentration was calculated using summed PILS concentrations of Na^+, Cl^-, and Mg^{2+} along with

198   the respective concentrations of the mass concentrations of K^+, Ca^{2+} and SO_4^{2-} in sea salt (0.037, 0.04 and 0.25,

199   respectively, by mass) (Crosbie et al., 2022).

200

201   **2.2.4 Aerosol Particle Classification**

202   Aerosol particle optical data were grouped depending on their AAE and SAE (Section 2.2.2) values and based on the

203   method of Cazorla et al. (2013), which used sun photometer measurements to arrive at the following classifications

204   as part of evaluating aircraft data over California, USA: coated large particles, dust and elemental carbon mix, dust

205   dominated, organic carbon and dust mix, organic carbon dominated, elemental carbon and organic carbon mix, mixed,

206   and elemental carbon dominated. This method has been used for cases when chemical composition is not available

207   (Höpner et al., 2019), and can be useful because the composition data from the AMS is limited to submicrometer

208   particles (0.06 to 0.6 μm vacuum aerodynamic diameter) while the f(RH) includes relatively larger particles (< 5 μm

209   dry diameter).

210

211   **2.2.5 Effective Particle Density**

212   Following Shingler et al. (Shingler et al., 2016b), effective particle density was calculated by dividing the sum of the

213   30 s total mass concentration from the AMS species (organics, SO_4^{2-}, NO_3^-, NH_4^+, and Cl^-) and 30 s averaged black

214   carbon from SP2 by the 30 s averaged integrated (for particles with diameter from 0.1 to 1 μm) volume concentration

215   from the LAS (Table 1).

216

217   **2.3 Modeling**

218

219   **2.3.1 Trajectory Analysis**

220   This work leverages trajectory results explained in detail by Hilario et al. (2021) using the National Oceanic and
221   Atmospheric Administration (NOAA) Hybrid Single Particle Lagrangian Integrated Trajectory Model (HYSPLIT)
222   (Stein et al., 2015; Rolph et al., 2017). Five-day HYSPLIT back trajectories from specific CAMP[2]Ex flight locations
223   were associated with air masses undergoing long-range transport from either the Maritime Continent (MC), East Asia
224   (EA), peninsular Southeast Asia (PSEA), or the West Pacific (WP) when they were within the regions at altitudes
225   below 2 km for more than 6 h. The back trajectories were generated based on 1-minute resolution aircraft locations
226   and 0.25° x 0.25° resolution NOAA Global Forecasting System (GFS) archived meteorological data. The source
227   regions are approximately within the following lowest and highest latitude and longitude values, respectively: MC (-
228   9.5° - 6.5° and 95° - 119°), EA (22° - 47° and 105° - 121.5°), PSEA (10° - 20° and 98° - 106 °), and WP (3°-25° and
229   120.5°-122.5°). The classification "Other" was used for back trajectories that either passed by the regions but at
230   elevations above the boundary layer (defined as 2 km), came from sources farther away than the four listed above,
231   were more localized to the Philippines, had too few sample counts, or were from stagnant air (Hilario et al., 2021).
232

233   **2.3.2 CAM-chem Model Configuration**
234   The Community Atmosphere Model with comprehensive tropospheric and stratospheric chemistry CAM-chem is used
235   here as the atmospheric component of the Community Earth System Model (CESM2). CAM-chem includes the modal
236   aerosol model (MAM4) (Liu et al., 2016) and results were evaluated with the CAMP[2]Ex AMS composition and f(RH)
237   observations for two case studies. Two CAM-chem simulations with different horizontal resolutions were performed
238   using the spectral element grid mesh and dynamical core. The grid mesh resolution for one simulation was uniform
239   with ~111 km (labeled ne30). The other simulation employed regional refinement over East Asia with grid spacing
240   ~27 km (labeled MUSICA) in the regionally refined region and ~111 km elsewhere across the globe; a configuration
241   as part of the Multi-Scale Infrastructure for Chemistry and Aerosols version 0 (MUSICAv0) (Schwantes et al., 2022).
242   More information about CAM-chem is in the supplementary section (S1).

244   In CAM-chem, aerosol hygroscopicity is represented with the kappa value (Petters and Kreidenweis, 2007) using the
245   mixing rule (Stokes and Robinson, 1966). Kappa was calculated from the CAM-chem Aitken (0.015 – 0.053 µm) and
246   accumulation mode (0.058 – 0.48 µm) outputs based on the volume fractions of the aerosol constituents (ε, Eq. 3) that
247   were derived from their densities (Table S1). The following internally mixed aerosol species from CAM-chem were
248   included in the analysis: organics (primary/hydrophobic, aged/hygroscopic, and secondary ($C_{15}H_{38}O_2$)), sulfate
249   (NH_4HSO_4), sea salt, dust ($AlSiO_5$), and black carbon (primary/hydrophobic and aged/hygroscopic) (Tilmes et al.,
250   2023). Some limitations in the calculation of kappa are that CAM-chem does not include nitrate aerosol, and that
251   constant kappa values for primary and aged organics based on past work (Table S1) were used, even if it is known
252   that kappa of organics varies with aging (Kuang et al., 2020). Kappa was also calculated from the submicrometer
253   AMS and SP2 observations using the assigned species properties for available aerosol species in CAM-chem: aged
254   organics, aged black carbon, and ammonium sulfate. Submicrometer sea salt and dust data are not available and were
255   not included in the calculation for submicrometer kappa from observations.

256
$$\kappa_{chem} = \sum \kappa_i \, \varepsilon_i \qquad\qquad (3)$$

257 To enable a corresponding evaluation based on actual aerosol hygroscopicity observations, the f(RH) from CAMP[2]Ex
258 were converted to kappa based on past studies (Brock et al., 2016b; Kuang et al., 2017; van Diedenhoven et al., 2022).
259 The approximate wet (80 %) and dry (20 %) relative humidity values of the scattering measurements were used to
260 convert f(RH) to an optical kappa (κ_{opt}) based on Equation 4 (Brock et al., 2016b; Kuang et al., 2017). This was
261 approximated from the proportional relationship between the aerosol scattering cross section (which is the basis of
262 f(RH)) and aerosol volume (the change of which is usually described as growth factor) which Brock et al. (2016b) in
263 their study had associated with kappa. The optical kappa was converted to the chemical kappa (κ_{chem}) based on the
264 slope of the relationship between κ_{opt} and κ_{chem} from Brock et al. (2016b). This method (Eq. 5) of converting κ_{opt} to
265 κ_{chem} was also used by van Diedenhoven et al. (2022) for the f(RH) data for CAMP[2]Ex and is associated with 40 %
266 uncertainty (van Diedenhoven et al., 2022). The derived chemical kappa values for bulk aerosol particles are compared
267 to the kappa calculated using the ZSR mixing rule from the submicrometer observations (AMS and SP2) and model
268 outputs.

269
$$f(RH) = \frac{1 + \kappa_{opt}\frac{RH_{wet}}{100 - RH_{wet}}}{1 + \kappa_{opt}\frac{RH_{dry}}{100 - RH_{dry}}} \qquad (4)$$

270
$$\kappa_{chem} \approx \frac{\kappa_{opt}}{0.56} \qquad (5)$$

271 **3. Results and Discussion**

272 **3.1 General Characterization of f(RH) for CAMP[2]Ex**

273 **3.1.1   Spatial Distribution of f(RH)**

274 The f(RH) values in the CAMP[2]Ex campaign (Fig. 1a) had an interquartile range of values between 1.05 and 1.42 and
275 were low (median of 1.24 for 143,107 1 s points) compared to other (Table 2) polluted marine environments (Titos et
276 al., 2021). We note that the comparisons to other studies may be affected by the slight difference in relative humidity
277 (f(RH=85 %/RH=40 % for Titos et al. (2021) and f(RH=82 ± 10 %/RH<40 % for this study) used to calculate f(RH).
278 The distribution of f(RH) and ambient RH values is narrowest in the lowest altitudes (< 3 km), where most of the
279 samples were taken (Fig. 1b). Both f(RH) and ambient RH distributions become broader at higher altitudes, where
280 there is a higher prevalence also for higher f(RH) values and lower ambient RH values. Broadening of the f(RH)
281 distribution at higher altitudes is at least partially attributed to lower dry scattering coefficients that result in increased
282 uncertainty in the calculation of f(RH). The different aerosol sources (Fig. 1a) in the region also contribute to the range
283 of measured f(RH), with transported emissions from more distant sources presumably more influential at the highest
284 altitude ranges.

285
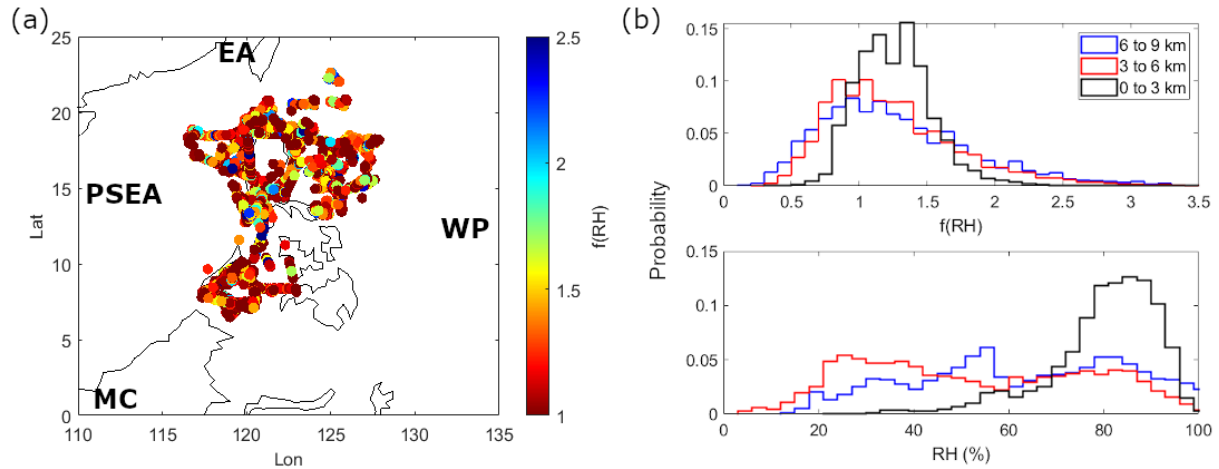
Figure 1. (a) Map showing flight locations during CAMP²Ex color coded by *f*(RH=82 % ± 10 %/RH<40 %) 1 s values at
550 nm and approximate locations of the air mass sources (black text) identified by Hilario et al. (2021) that affected
CAMP²Ex: Maritime Continent (MC), East Asia (EA), peninsular Southeast Asia (PSEA), and the West Pacific (WP)
(PSEA is farther west at ~105°E and EA extends farther north) of air mass sources (Hilario et al., 2021) around the region.
(b) Histograms of *f*(RH=82 % ± 10 %/RH<40 %) at 550 nm and ambient relative humidity (RH) for three altitude bins
with the following counts: $n_{(0\ to\ 3\ km)}$: 139,026, $n_{(3\ to\ 6\ km)}$: 10,321, and $n_{(6\ to\ 9\ km)}$: 7,260.

The lowest median *f*(RH) (1.05 with Q1 and Q3 of 0.94 and 1.2) is from air masses traced to the MC (Fig. 2a), which

coincide with influence from smoke particles, similar to values recorded in past studies from aged biomass (Table 2).

The air mass from EA (Fig. 2a) has the narrowest range of values (Q1: 1.28, median (Q2): 1.38, Q3: 1.47) compared

to other air masses, likely representative of urban aerosol particles (Table 2). The highest median *f*(RH) (1.49 with Q1

and Q3 of 1.26 of 1.73) are from air masses with back trajectories from the WP (Fig. 2a), likely due to marine aerosol

particles interacting with particles from the MC and other regional sources. This mixing of the otherwise clean marine

air with regional pollution sources effectively decreases aerosol hygroscopicity and this type of environment is often

called a polluted marine environment (Titos et al., 2021).

Table 2: Hygroscopicity values of various aerosol types based on selected summary studies for measured *g*(RH)
(Swietlicki et al., 2008) and *f*(RH) (Eldering et al., 2002; Doherty et al., 2005; Liu and Li, 2018; Dumka et al.,
2017; Gogoi et al., 2015; Burgos et al., 2019; Titos et al., 2021), modeled κ (Pringle et al., 2010), and measured
***f*(RH) for identified air masses affecting CAMP²Ex (Hilario et al., 2021): Maritime Continent (MC), East Asia**
(EA), peninsular Southeast Asia (PSEA), West Pacific (WP), and Other, categorized by associated aerosol
source.

Aerosol Type	Past Studies			Air Masses Affecting CAMP²Ex
	g(RH=90%)* (10 - 500 nm)	f(RH=85%/RH=40%)** (< 1000 nm)	κ**** (5 - 500 nm)	f(RH=82 ± 10 %/RH<40%)** (< 5000 nm)
Clean Marine	1.62 - 2.14	2.10 - 2.30	0.92	1.49 (WP)
Polluted Marine	1.00 - 1.76	1.73 - 2.20	0.59	1.23 (Other)
Urban Continental	1.00 - 1.68	1.38 - 1.60	0.21 - 0.36	1.20 - 1.38 (EA, PSEA)
Aged Biomass	1.15 - 1.30	1.02 - 2.1***	< 0.1	1.05 (MC)

306 Most (98 %) of the f(RH) data were calculated for observations below 3 km (Fig. 2b), due to the relatively clean free

307 troposphere in the region. Median f(RH) values generally decrease with altitude in the lower 3 km. An increase in

308 median f(RH) is observed between 4 – 6 km (median from 1.14 to 1.32), where the contribution of the mixed air mass

309 ("Other") is most dominant. The f(RH) values decrease above 6 km to the lowest median f(RH) (1.07) between 8 – 9

310 km, where air masses are generally from Other and the MC.

311 Latitudinally (Fig. 2c), f(RH) is lowest nearest Borneo in the MC (median of 0.95 to 1.07 in the regions from 6.85° N

312 – 10.25° N), coincident with the dominant influence of biomass burning. There were active fires in the area during the

313 time samples were taken from this latitude. f(RH) is highest in the northern Philippines (median of 1.33 to 1.44 in the

314 regions from 18.75° N – 22.15° N), where the influence of WP and EA air was most prevalent. This is consistent with

315 the longitude data (Fig. 2d), which exhibit the lowest f(RH) values for longitudes (median of 1.02 to 1.18 in the regions

316 from 117.95° E – 120.55° E) that had the highest MC contribution. The highest f(RH) is observed in longitudes

317 (median of 1.38 to 1.40 in the regions west of 116.65° E and east of 123.15° E) that were more associated with the

318 northern Philippines (Fig. 1a). To delve deeper into our analysis, we discuss next the size and composition data.

320
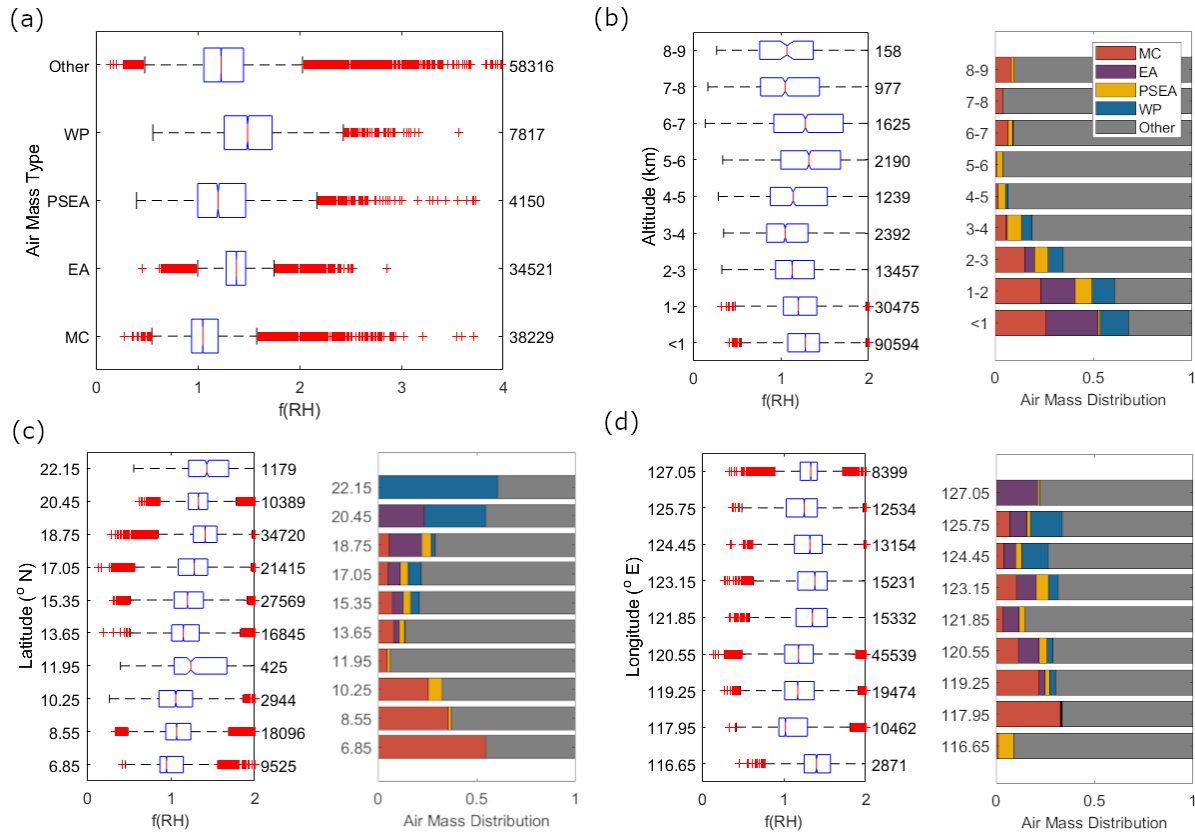
Figure 2. Distribution of *f*(RH=82 % ± 10 %/RH<40 %) 1 s data at 550 nm during the CAMP²Ex field campaign for relevant (a) air masses, (b) altitude, (c) latitude, and (d) longitude levels and corresponding stacked bars of air mass contributions for panels b - d. The (a) air mass types are from Hilario et al. (2021). The numbers to the right of the notched boxplots (boxes correspond to the 25th to 75th percentile of the data, the red line is the 50th percentile, the whiskers represent 1.5 * the interquartile range, the red crosses are the outliers, and when the notches in the boxplots do not overlap there is 95 % confidence that the medians of the boxplots are different) are the counts, and the (b – d) bars to the right of the boxplots show the fractional contribution of each air mass type to the total number of air masses in the specific location. The y-values for (c-d) latitude and longitude are the midpoints of the specific coordinate bins.

3.1.2   *f*(RH) Relationships with Size and Composition

The relative size of particles per air mass can be inferred from the extinction Ångström exponent (AE), which relates the extinction of light at specific wavelengths to particle size (Ångström, 1929). Since scattering is the dominant component of extinction, the scattering Ångström exponent (SAE) is often used to relate to particle size, where larger SAE suggests smaller particles. The median SAE values (Fig. 3a) are similar and between 2.09 (MC with Q1 and Q3 of 1.92 and 2.26) to 2.16 (Other with Q1 and Q3 of 1.75 and 2.32) for four of five air masses, indicative of smaller particles. The WP has a median value of 1.37 (with Q1 and Q3 of 1.05 and 1.88), suggestive of the presence of a mixture of accumulation-mode and coarse-mode particles (SAE < 1 occurs for large particles like sea salt and dust) (Schuster et al., 2006; Bergstrom et al., 2007). Past studies have suggested that biomass burning particles exhibit SAE values greater than 1.4, which does not discount the fact that most of the *f*(RH) data collected during CAMP²Ex are possibly impacted by biomass burning.
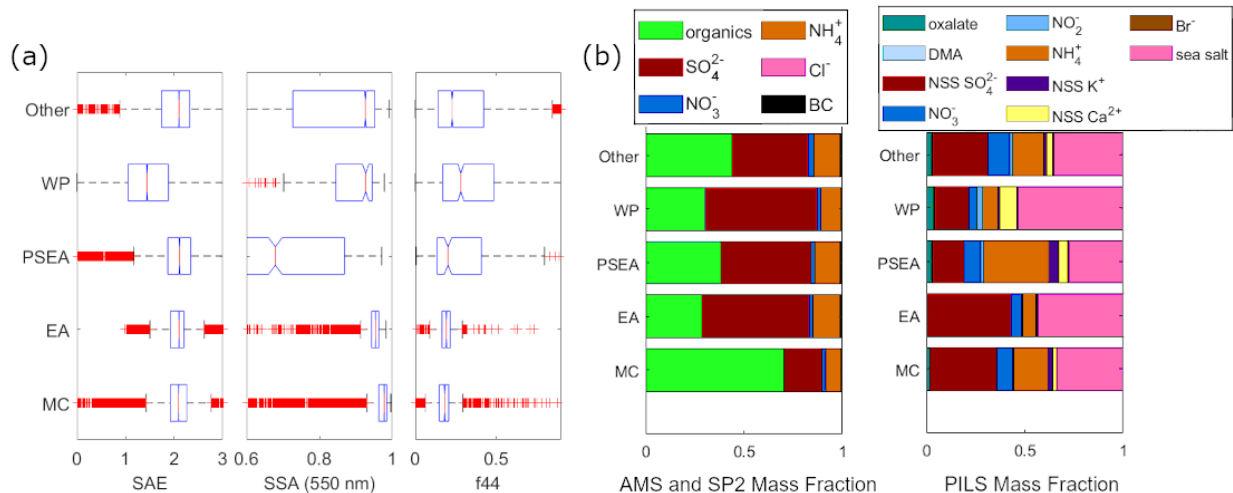
Figure 3. Physicochemical properties of air masses. (a) Boxplots (boxes correspond to the 25th to 75th percentile of the data, the red line is the 50th percentile, the whiskers represent 1.5 * the interquartile range, the red crosses are the outliers, and when the notches in the boxplots do not overlap there is 95 % confidence that the medians of the boxplots are different) of scattering Ångström exponent (SAE), single scattering albedo (SSA, 550 nm), and ratio of the mass spectral marker m/z 44 marker relative to total organic mass (f_{44}) and (b) (left) submicrometer mean aerosol mass spectrometer (AMS) derived organic, SO_4^{2-}, NO_3^-, NH_4^+, and Cl^- and soot photometer (SP2) derived black carbon (BC) mass fractions and (right) bulk (< 5 µm) mean particle-into-liquid sampler (PILS) and ion chromatograph derived oxalate, dimethylamine (DMA), non-sea salt SO_4^{2-}, NO_3^-, NO_2^-, NH_4^+, non-sea salt K^+, non-sea salt Ca^{2+}, Br^-, and sea salt mass fractions per air mass: Maritime Continent (MC), East Asia (EA), Peninsular Southeast Asia (PSEA), West Pacific (WP), and Other (Hilario et al., 2021).

One of the indicators of biomass burning in Southeast Asia is organic matter (Adam et al., 2021). The MC air mass (Fig. 3b) has the greatest (71 %) mass fraction of organics among the air masses and the highest median SSA (0.98 with Q1 and Q3 of 0.96 and 0.99) (Fig. 3a) that suggests more scattering, rather than absorbing, particles (Moosmüller and Sorensen, 2018). This is consistent with observations from field work in tropical peatland fire in Southeast Asia, where particles were mostly from smoldering combustion and were moderately absorbing, with brown carbon dominating absorbance (Stockwell et al., 2016). Smoldering combustion, which is more common in the Maritime Continent (Reid et al., 2013), is known to produce less elemental carbon (Reid et al., 2005) and potassium (Robinson et al., 2004) compared to flaming combustion. Biomass burning activities were active in the MC during the field campaign (Reid et al., 2023). The MC air mass also has the lowest f_{44} median values (0.18 with Q1 and Q3 of 0.15 and 0.21) (Fig. 3a) suggesting it is the least-oxidized and least photochemically-aged air mass and thus closest to the source compared to other air masses. Chen et al. (2022) who studied tropical peat smoldering (similar to those in MC) showed that primary organics were not oxidized (f_{44} < 0.02) while secondary organics were highly oxidized, that oxidation increases f_{44} (oxidized organics: 0.01 < f_{44} < 0.11), and that high RH speeds up the oxidation process especially for smaller particles (~100 nm) (Chen et al., 2022). In the U.S., as another example, f_{44} from wildfire plumes up to 8 hours old did not exceed 0.12 (Garofalo et al., 2019). The high RH during CAMP²Ex (Fig. 1b) likely led to the increased oxidation of secondary organics resulting in median f_{44} values that are relatively high (for all air masses even in MC), suggesting that most of the particles sampled during CAMP²Ex are aged. The high organic mass fraction is consistent with the MC having the lowest median f(RH) as organics are known to reduce aerosol hygroscopicity (Kalberer, 2014; Sorooshian et al., 2017; Shingler et al., 2016a).

369   There is an inverse relationship between hygroscopicity and organic mass fraction data that is most evident in f(RH)
370   values collected within the boundary layer (< 3 km) during CAMP²Ex (Fig. 4a). Those data points that have the highest
371   organic mass fraction values (> 0.6) are also associated with CO concentrations (> 250 ppb) that are typically
372   associated with biomass burning (Shingler et al., 2016a) and are mostly from the MC area (Fig. 4b). The relationship
373   between f(RH) and organic mass fraction during CAMP²Ex is similar to those in the Indian ocean during INDOEX
374   (based on the sloped of calculated f(RH) from estimated γ and organic mass fraction) (Quinn et al., 2005), which is
375   similarly affected by the outflow of biomass burning. The slope of the inverse relationship between f(RH) and organic
376   mass fraction is most steeply negative (-0.81) for the air masses coming from EA (Fig. 4c). This slope for the air
377   masses coming from EA is less steep than the f (RH=85 %/RH=40 %) at 550 nm to organic mass fraction relationship
378   (-1.20 ± 0.04) from a ground station in the populated and growing region of the Yangtze River Delta in China (Zhang
379   et al., 2015), where organic contributions are lower and mean f(RH) values are higher (1.58 ± 0.12) than the median
380   f(RH) (1.38) during CAMP²Ex for air massed coming from EA.

381
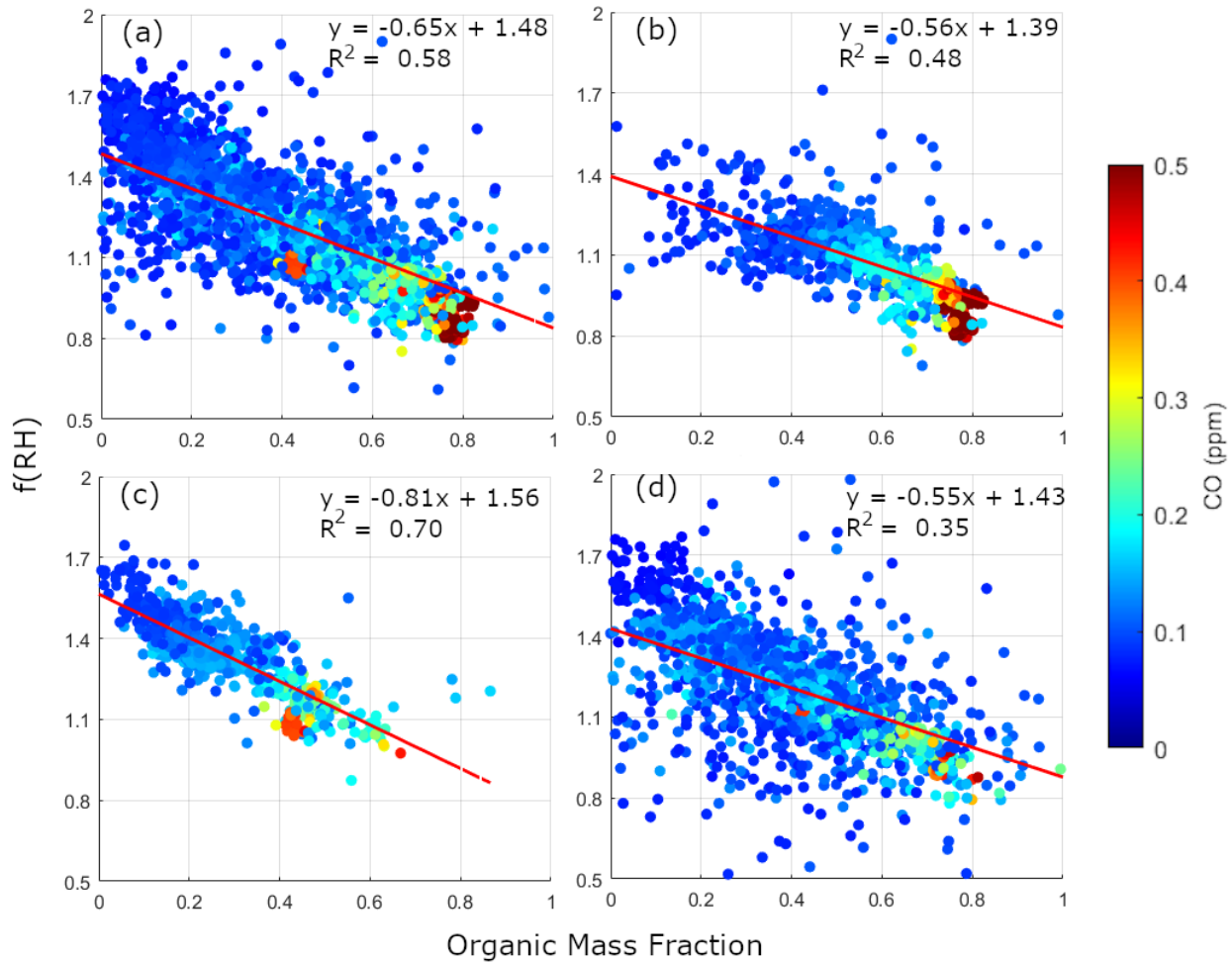
382   **Figure 4. Effect of organic mass fraction on f(RH). (a-d) Scatter plots of 30 s averaged f(RH=82 % ± 10 %/RH<40 %) at**
383   **550 nm and corresponding organic mass fraction contribution to total submicrometer aerosol mass (sum of organic, SO₄²⁻,**
384   **NO₃⁻, NH₄⁺, Cl⁻, and black carbon (BC) mass concentration) and (red) linear regression line and (upper right)**

385 **corresponding equation and goodness of fit for (a) all data collected at altitudes below 3 km and (b-d) for air masses coming**
386 **from (b) the Maritime Continent (MC), (c) East Asia (EA), and (d) Other. The dots are colored by their CO concentration.**

387 The highest median f(RH) values are from the WP and EA air masses (Fig. 2a). Both have lower organic mass

388 fractions (0.29 and 0.30, respectively) compared to other air masses and are therefore expected to have higher f(RH)

389 based on Fig. 4. The WP air masses have coarser particles, based on their SAE values (Fig. 3a), and have a marine

390 origin (with higher DMA mass fraction, Fig. 3b) with high sea salt fraction (54 %, Fig. 3b), contributing to it having

391 the highest median f(RH) amongst the air masses. The WP air masses appear to have interacted with aged organic

392 particles from biomass burning and industry including fine absorbing particles potentially from industry and dust

393 owing to its relatively high median f_{44} (0.26 with Q1 and Q3 of 0.17 and 0.48) and low median SSA (0.93 with Q1

394 and Q3 of 0.85 and 0.95). Particles with predominantly clean marine sources tend to have higher (≥ 0.97) SSA

395 (Dubovik et al., 2002), thus the WP data suggest a polluted marine source (Lacagnina et al., 2015). Though, we note

396 that the air masses from the WP have relatively low scattering and absorption coefficients and that these could have

397 affected the calculations for SSA. EA air exhibits the highest non-sea salt sulfate mass fraction (0.43) (Fig. 3b) that,

398 along with its predominantly fine particle size and median SSA (0.95 with Q1 and Q3 of 0.94 and 0.96), strongly

399 suggests that it was transported from an urban source. Sulfate is a known industrial product of East Asia (Smith et al.,

400 2011; Li et al., 2017; Lorenzo et al., 2023).

401 Particles from PSEA have the lowest median SSA (0.68 with Q1 and Q3 of 0.55 and 0.87) (Fig. 3a). This suggests the

402 presence of more absorbing particles relative to scattering, possibly including elemental carbon and aged dust. Based

403 on the PSEA air masses having the highest non-sea salt potassium mass fraction (0.05, Fig. 3b) the particles could be

404 from biomass burning. It is well-documented that dust can be entrained in smoke plumes due to reasons such as

405 turbulent mixing around flames and burn fronts (Palmer, 1981; Kavouras et al., 2012; Maudlin et al., 2015; Schlosser

406 et al., 2017). Dust from East Asia and biomass burning from PSEA have been observed to be mixed in the boreal

407 spring in Taiwan (Dong et al., 2018), and though CAMP[2]Ex sampled during a different season, it is still possible that

408 this mixing of East Asian dust and PSEA biomass burning could have occurred and impacted the CAMP[2]Ex region

409 during the field campaign.

(a)   (b)

410
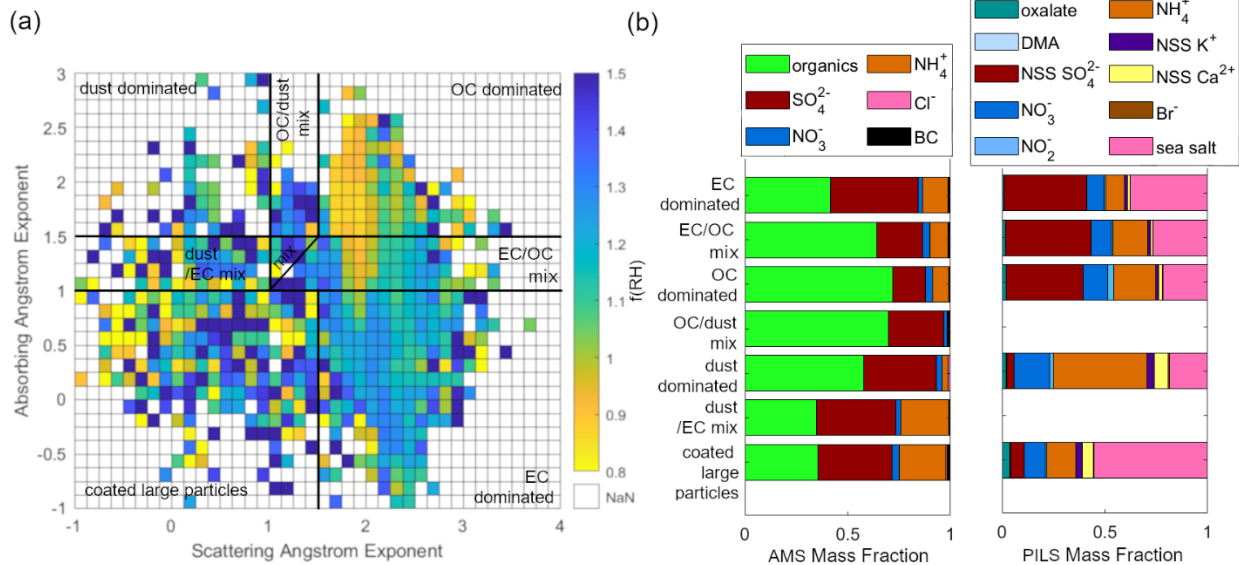
Figure 5. Aerosol types based on particle optical data. (a) Median f(RH =82 % ± 10 %/RH<40 %) at 550 nm of data points with absorbing Ångström Exponent (AAE, 470-660 nm) and scattering Ångström Exponent (SAE, 450-700 nm) values that correspond to suggested aerosol types from past studies (Cazorla et al., 2013) with following counts and bulk median f(RH=82 % ± 10 %/RH<40 %) per aerosol type: EC dominated (16,908 and 1.19), EC/OC mix + mix (20,686 and 1.03), OC dominated (1942 and 0.94), OC/dust mix (55 and 1.31), dust dominated (79 and 1.15), dust/EC mix (204 and 1.12), and coated large particles (729 and 1.21). (b) (left) Submicrometer mean organic, SO_4^{2-}, NO_3^-, NH_4^+, Cl^-, and black carbon (BC) mass fractions and (right) available bulk (< 5 µm) oxalate, dimethylamine (DMA), non-sea salt SO_4^{2-}, NO_3^-, NO_2^-, NH_4^+, non-sea salt K^+, non-sea salt Ca^{2+}, Br^-, and sea salt mass fractions per aerosol type.

Using the AAE and SAE with categorization determined by Cazorla et al. (2013), the f(RH) can be related to the types of aerosols. Note that the median f(RH) values for the aerosol types may be slightly different than the raw 1 s f(RH) data because the median f(RH) is only calculated for the aerosol types when both the scattering and absorbing Ångström Exponent values are available. The highest median f(RH) of 1.31 (with Q1 and Q3 of 0.89 and 1.46) and 1.21 (with Q1 and Q3 of 0.88 and 1.68) are from the OC/dust mix and coated large particles aerosol types (Fig. 5), respectively, though there are only 55 data points for the OC/dust mix so the aerosol classification for it may not be as robust. The high f(RH) for the coated large particles is consistent with its largest bulk sea salt mass fraction (0.56) (Fig. 5b) compared to other aerosol types, though they only make up 1.8 % of the total number of particles. Dust dominated particles make up only 0.05 % of the total number of particles and had the highest non-sea salt calcium and a median f(RH) of 1.15 (with Q1 and Q3 of 0.94 and 1.43).

Most of the aerosol particles (< 5 µm dry diameter and 93 % of all particles) collected during the CAMP[2]Ex field campaign have optical properties (Fig. 5a) that resembled EC/OC mix + mix (in this case we combined the sub-categories of EC/OC mix and mix) (51 %) and EC dominated (42 %) aerosol types. These carbonaceous particles are less hygroscopic, and their dominance helps to explain the low median f(RH) in the CAMP[2]Ex region. The EC dominated particles have the third highest median f(RH) at 1.19 (with Q1 and Q3 of 1.05 and 1.33), which is unusual because EC is known to be hydrophobic. Compositional data sheds some light on this, because the particles classified as EC dominated have higher submicrometer sulfate (0.43) and bulk sea salt (0.38) mass fractions (Fig. 5b) compared to particles classified as OC (0.16 and 0.22) and dust dominated (0.35 and 0.19), which are known to have low

437 hygroscopicity in general. This mixing of sulfate and sea salt with EC dominated particles increases their bulk *f*(RH).

438 The EC dominated particles come from the EA, MC, and Other air masses. East Asia is a known sulfur source and

439 shipping contributes to sulfate in the region (Miller et al., 2023). Peat smoke particles from MC have also been found

440 in past studies to have sulfate mixed with carbonaceous species (Nakajima et al., 1999), where up to ~20 % of the

441 mass fraction of secondary organic aerosol from lab experiments on peat burning was attributed to sulfate (Chen et

442 al., 2022).

443 The OC dominated type has the highest submicrometer organic mass fraction (0.72) and a median *f*(RH) of 0.94 (with

444 Q1 and Q3 of 0.85 and 1.06), which is consistent with the expected effect of organics to lower hygroscopicity. The

445 median *f*(RH) values below 1, though, are counterintuitive given that the presence of moisture in the region is thought

446 to generally increase the particle size and consequently the amount of aerosol light scattering. Data where *f*(RH) is

447 less than unity have been observed in past studies due to a number of suspected factors including (but not limited to)

448 volatilization effects, changes in optical properties during humidification, and particle restructuring (Shingler et al.,

449 2016b).

450

451
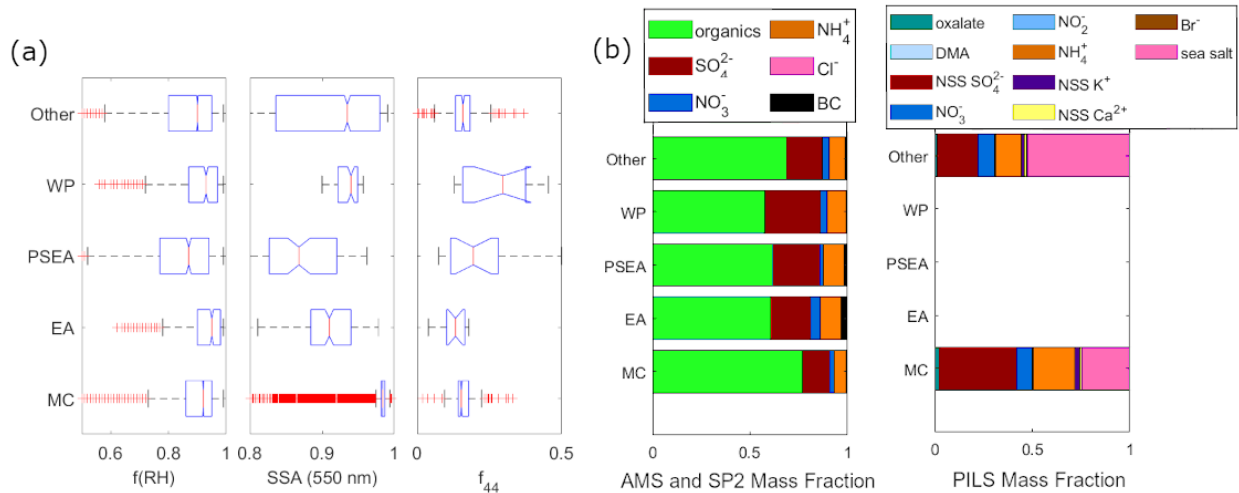
452 **Figure 6. Physicochemical properties of air masses with sub-1 *f*(RH) at 550 nm. (a) Boxplots (boxes correspond to the 25th**
453 **to 75th percentile of the data, the red line is the 50th percentile, the whiskers represent 1.5 * the interquartile range, the red**
454 **crosses are the outliers, and when the notches in the boxplots do not overlap there is 95 % confidence that the medians of**
455 **the boxplots are different) of 1 s *f*(RH=82 % ± 10 %/RH<40 %) < 1 (MC: 14,612, EA: 473, PSEA: 986, WP: 483, and Other:**
456 **9919 counts) and the corresponding single scattering albedo (SSA, 550 nm) and ratio of the mass spectral marker m/z 44**
457 **marker relative to total organic mass (f44) and (b) (left) submicrometer mean organic, SO4^2-, NO3-, NH4+, Cl-, and black**
458 **carbon (BC) mass fractions and (right) available bulk (< 5 μm) oxalate, DMA, non-sea salt SO4^2-, NO3-, NO2-, NH4+, non-**
459 **sea salt K+, non-sea salt Ca2+, Br-, and sea salt mass fractions per regional air mass (Hilario et al., 2021) for times with**
460 ***f*(RH=82 % ± 10 %/RH<40 %) < 1.**

461 To investigate aerosol characteristics when *f*(RH) is < 1, we plot the f(RH) box plots from each of the regions for data

462 points where *f*(RH) < 1 (Fig. 6a). There are several instances (26,473 times or 19 % of the time for the whole campaign)

463 when the *f*(RH) was below 1. In general, 30 s resolution organic mass fractions greater than 0.75 correspond to sub-1

464 *f*(RH) (Fig. 4a). The most prevalent regional air mass association for sub-1 *f*(RH) is with the MC air masses (*f*(RH) <

465   1 from the MC was 56 % of all data). The mean organic mass fraction is dominant (0.57 – 0.77) and almost doubled

466   compared to the whole campaign (Fig. 3b), for all the air masses with sub-1 f(RH) (Fig. 6b). Mean organic mass

467   fraction is highest for the MC (0.77) air mass. The organics from the sub-1 f(RH) data are the least aged throughout

468   the campaign for the MC, PSEA, and Other air masses (Fig. 6a). The CAMP²Ex data offer an opportunity to inspect

469   the prevalence of such values and to see what factors coincide with such situations. However, the unique sample make-

470   up of the particles in the CAMP²Ex region makes other reasons, including sample losses due to volatilization, also

471   plausible (Reid et al., 2023). Shingler et al. (Shingler et al., 2016b) also observed such sub-1 values for both f(RH)

472   and the humidified diameter growth factor g(RH) in air masses enriched with carbonaceous components over North

473   America.

474   The most dominant aerosol types for the sub-1 f(RH) data are the carbonaceous ones (96 %) (Fig. 5b), with the EC/OC

475   component contributing the most: EC/OC mix + mix (the combined sub-categories of EC/OC mix and mix) (68 %),

476   EC-dominated (18 %), and OC-dominated (10 %). Both bulk ammonium and sulfate mass fractions for the MC also

477   are higher for the sub-1 f(RH) cases (Fig. 6b) compared to the whole campaign (Fig. 3b, PILS), while the bulk sea salt

478   mass fraction was lower. The bulk sea salt mass fraction of the Other category (Fig. 6b) increases for the sub-1 f(RH).

479   Most of the particles contributing to the sub-1 f(RH) are fine particles (median Ångström Exponent ~2, Fig. 6a) with

480   more reflective characteristics (SSA ≥ 0.90) compared to data for the entire campaign. To understand more about sub-

481   1 f(RH), we will look at a selected case in the succeeding section.

482   **3.2   Case Studies**

483   **3.2.1 Sub-1 f(RH) from Biomass Burning Smoke**

484   The chosen case study is part of a flight on 16 September 2019 that occurred closest to the Maritime Continent, which

485   is the source of the air masses that had the most counts of sub-1 f(RH) (Section 3.1.2). This flight coincided with an

486   active biomass burning event on 14 September 2019 (NASA, 2020) and fire hotspots in the Maritime Continent were

487   numerous throughout September 2019 (Othman et al., 2022). The back trajectories at 01:00 UTC, when the aircraft

488   began to make measurements closest to the surface (~300 m altitude) and perpendicular to the wind, all come from

489   the southwest of the aircraft location (Fig. 7a), in the direction from where biomass burning emissions were being

490   transported. Details about the flight and conditions during this case study are found in Crosbie et al. (2022). In their

491   study they note the smoke to be from Kalimantan with an age between 48 and 72 h. Consistently low f(RH) (all below

492   1, Fig. 7b) values were observed for a little less than an hour, until the aircraft began its ascent (Fig.7b). The aerosol

493   mass concentrations of >70 µg m^{-3} were among the highest in the entire field campaign and were dominated by

494   organics (Fig. 7b).

495
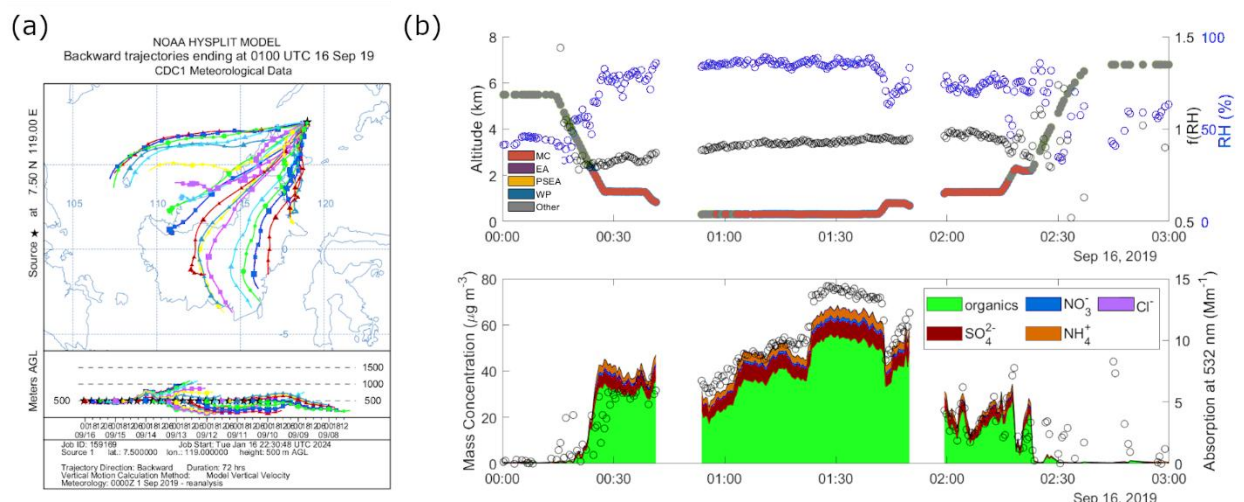
Figure 7. Case study of sub-1 *f*(RH=82 % ± 10 %/RH<40 %) at 550 nm on 16 September 2019. (a) Five-day back trajectories at the approximate flight location at 01:00 UTC. (b) (top) Time series plots of altitude colored by regional air mass, *f*(RH) in black circles, and RH (blue circles), and (bottom) aerosol mass concentrations from the AMS and absorption at 532 nm (black circles) during one of the flight legs closest to the surface from 00:00 to 03:00 UTC.

The sub-1 *f*(RH) during the lowest altitudes of the aircraft, from 01:00 to 01:40 UTC, are correlated with approximations of the submicrometer particle effective density (Fig. 8a). Absorption measurements along with back trajectories linked to active fires point to the increasing presence of EC and brown carbon with increasing particle density (even if there were no valid EC measurements for this specific time). Submicrometer number concentration, dry absorption (532 nm), organic mass fraction, and single scattering albedo are highest for the smallest effective density values for sub-1 *f*(RH) (Fig. 8b) during the entire campaign, likely due to the presence of EC and OC. This is consistent with the most dominant aerosol type during the field campaign, which is a mix of elemental and organic carbon based on SAE and AAE values. The dataset cannot be used to prove particle restructuring and very likely the sub-1 *f*(RH) values are due to other factors since particles' history included passes through humid areas where restructuring presumably would have already occurred prior to reaching the aircraft. In addition, smoldering from peat, which is dominant in the MC fires (Reid et al., 2023), is known to produce homogenous spheres, with no voids, that are similar to OC particles (Pokhrel et al., 2021), making restructuring unlikely to be the dominant mechanism to explain our findings. However, we present these results for the sake of documenting a Southeast Asia case of these unusual events occurring in EC/organic-rich air masses similar to past work (e.g., Shingler et al., 2016b and references therein) to emphasize that these events occur throughout the world and to motivate more research into the matter.

515
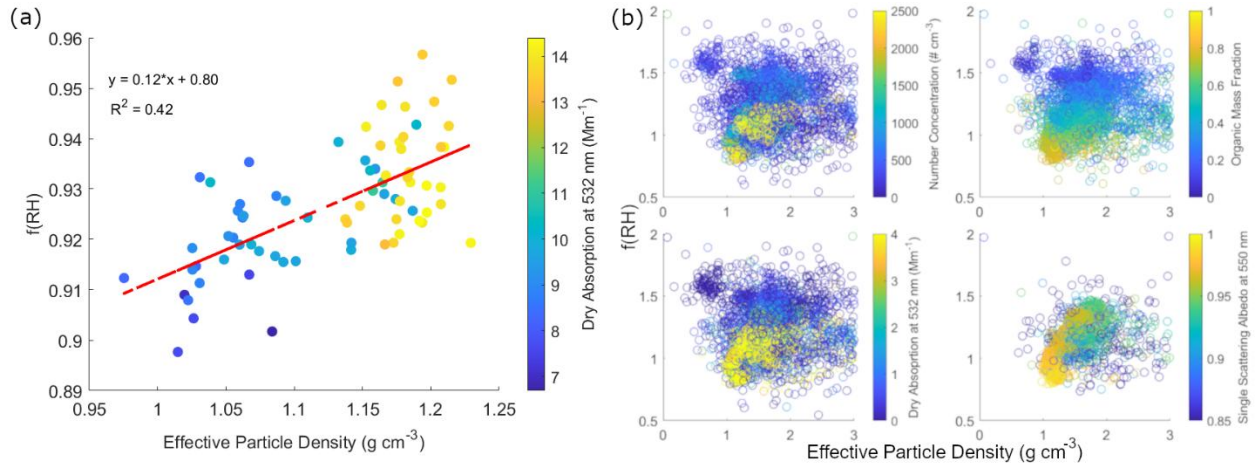
Figure 8. Effective particle density and *f*(RH). 30 s *f*(RH=82 % ± 10 %/RH<40 %) at 550 nm and effective particle density plots for (a) 16 September 2019 from 01:00 to 01:40 UTC colored by dry absorption at 532 nm and with (red) linear regression line and (upper left) corresponding equation and goodness of fit, and (b) for the entire CAMP²Ex field campaign and colored by (clockwise from top left) LAS number concentration of particles with diameters between 100 and 1000 nm, organic mass fraction, single scattering albedo at 550 nm, and dry absorption at 532 nm.

Smoke particles are known to have a range of density values, depending on their degree of atmospheric aging, affecting their size, and the processes they undergo. The effective particle density is usually lower for biomass burning particles from smoldering that have larger diameters (Pokhrel et al., 2021), compared to flaming. Freshly emitted smoldering particles have effective densities from 1.03 g cm⁻³ to 1.21 g cm⁻³ that do not vary much with diameter based on a laboratory study (Pokhrel et al., 2021). Our calculated values fall within this range (Fig. 8). This adds confidence to our observation that organics (brown carbon), which dominate smoldering emissions, are the major contributors to the sub-1 *f*(RH). Both aerosol hygroscopicity and effective particle density are important for properly modeling cloud condensation nuclei, one of the most important factors in aerosol-cloud interactions.

3.2.2 Vertical Transport

The vertical distribution of aerosols affects cloud formation, we investigate this through two cases of aerosol vertical transport. The vertical transport cases were identified from averages of the available vertical profiles made during CAMP²Ex. A large-scale event (01:53 to 06:20 UTC 20 Sep 2019) north of Luzon, Philippines, due to a tropical cyclone, and a smaller-scale event (02:55 to 06:02 UTC 24 Sep 2019) east of Luzon, due to shallow convection were chosen for the case studies. The measured median CO mixing ratio was used as a tracer for vertical transport (Kar et al., 2004). An increase in the median CO mixing ratio at higher altitudes along with multi-level winds from a similar direction were the main criteria used to identify the cases.

Northerly to northwesterly winds are the dominant source for the first case (Fig. 9a) influenced by tropical cyclone Tapah (TC Tapah's center was ~600 km northeast of the aircraft location). This suggests the influence of East Asia on the sample as described in Crosbie et al. (2022), where the meteorology is discussed in more detail. There is a general decrease in *f*(RH) from the lower levels that follows a similar trend to the decrease in total mass (Fig. 9b) and

541   sulfate mass fraction. Sulfate is hygroscopic so it is understandable that the f(RH) decreased with altitude as the sulfate

542   mass fraction decreased. The increase in CO between 6-7 km (Fig. 9b) suggests vertical transport aloft and was

543   accompanied by a subsequent decrease in f(RH) and ammonium mass fraction and increase in organic mass fraction

544   (Fig. 9b) between 6-8 km. This is consistent with analysis in previous sections, which show decreased f(RH) with

545   increased organic mass fractions.

546   Accompanying the general decrease of f(RH) with altitude are decreasing submicrometer median volume size

547   distribution (VSD) magnitudes and volume weighted average diameters (Fig. 10). Possible reasons for these trends

548   are that larger hygroscopic particles, such as sulfate (which make up the largest mass fraction at lower levels), were

549   scavenged (especially at lower altitudes) and/or activated into cloud drops, leaving the smaller particles behind.

550   Submicrometer aerosol mass also decreases with altitude, with values below 1 µg m^{-3} (Fig. 9b). There is a slight

551   increase in VSD magnitude from 6-8 km compared to 4-6 km, and especially at larger diameters, broadening the VSD

552   curve which may suggest cloud processing (Eck et al., 2012). Though sulfate enhancements have traditionally been

553   the marker for cloud processes (Barth et al., 2000; Faloona, 2009), more recent studies have observed potential cloud

554   processing cases with increased organics (i.e. Wonaschuetz et al., 2012; Dadashazar et al., 2022). This case could

555   thus be showing vertically transported organic matter that has possibly affected or was affected by the clouds between

556   6-7 km. Another observation is the increase of ammonium and nitrate mass fractions above 4 km (Fig. 9b). There is

557   no corresponding valid f(RH) data, and we can only infer based on the CO profile that begins to shift toward a more

558   positive slope with increasing altitude that this increase in ammonium could also be associated with cloud processing.

559   Ammonia is abundant in East Asia (Pawar et al., 2021) and although there are still limited studies, the scavenging

560   efficiencies of organics and ammonium (compared to sulfate) could also be contributing to their increasing mass

561   fractions with altitude (Yang et al., 2015; Hilario et al., 2025).
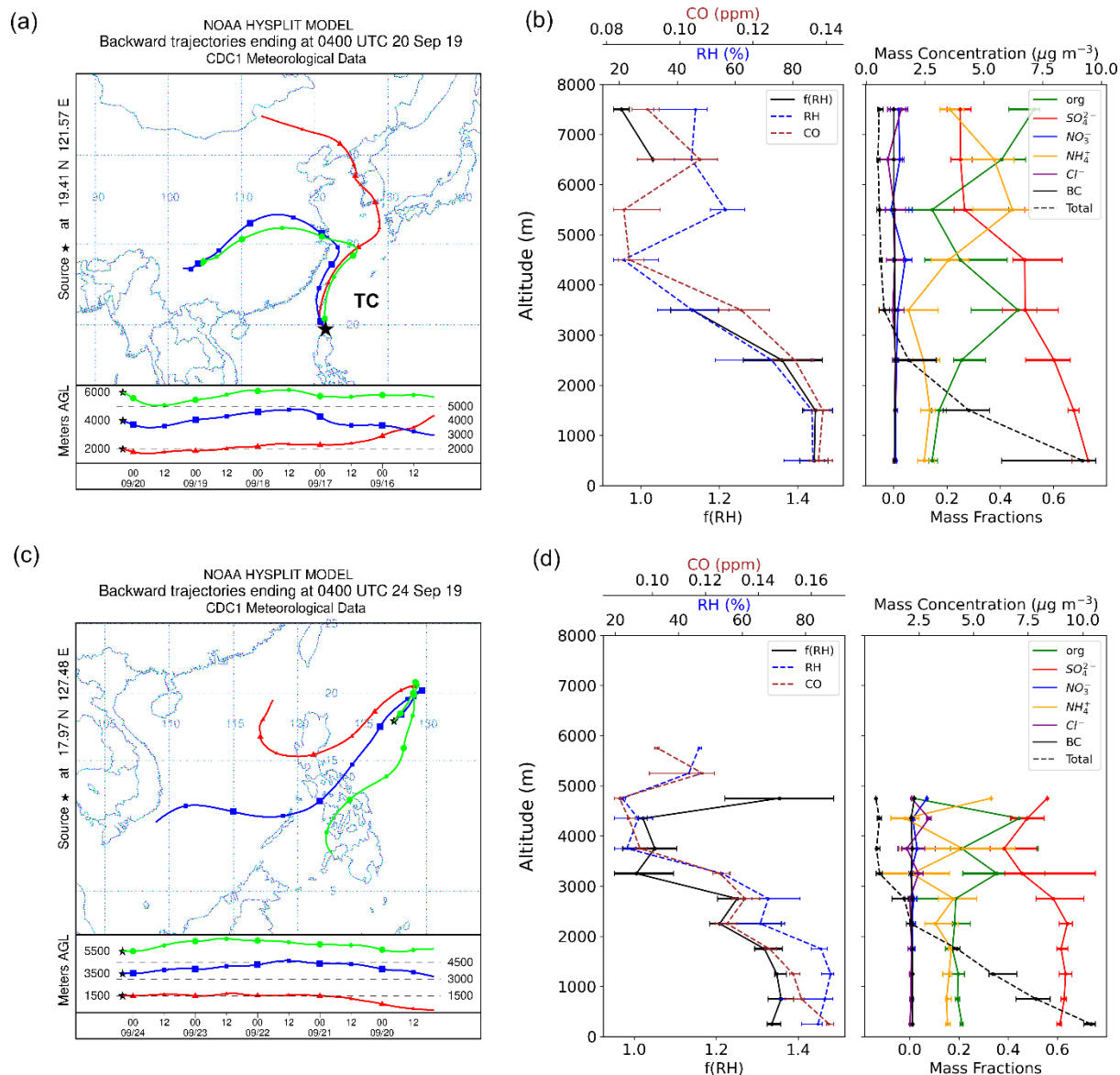
Figure 9. Case studies of (a-b) tropical cyclone-induced convection on 20 September 2019 and (c-d) shallow convection on 24 September 2019. (a) Five-day multi-level back trajectories from the average location of the aircraft from 01:53 to 06:20 UTC with the approximate TC center location and (b) vertical profiles (median, 25 and 75th percentiles) of (left) f(RH=82 % ± 10 %/RH<40 %) at 550 nm, relative humidity (RH), and CO mixing ratio and (right) submicrometer mass fractions of organics, sulfate, nitrate, ammonium, and black carbon and sum of mass concentrations from AMS and SP2 (dashed black line) for 1 km altitude bins, (c) five-day multi-level back trajectories from the average location of the aircraft from 02:55 to 06:02 UTC, and (d) vertical profiles of f(RH=82 % ± 10 %/RH<40 %) at 550 nm, relative humidity (RH), CO mixing ratio, and submicrometer mass fractions and sum of mass concentrations from AMS and SP2 for 0.5 km altitude bins.

572
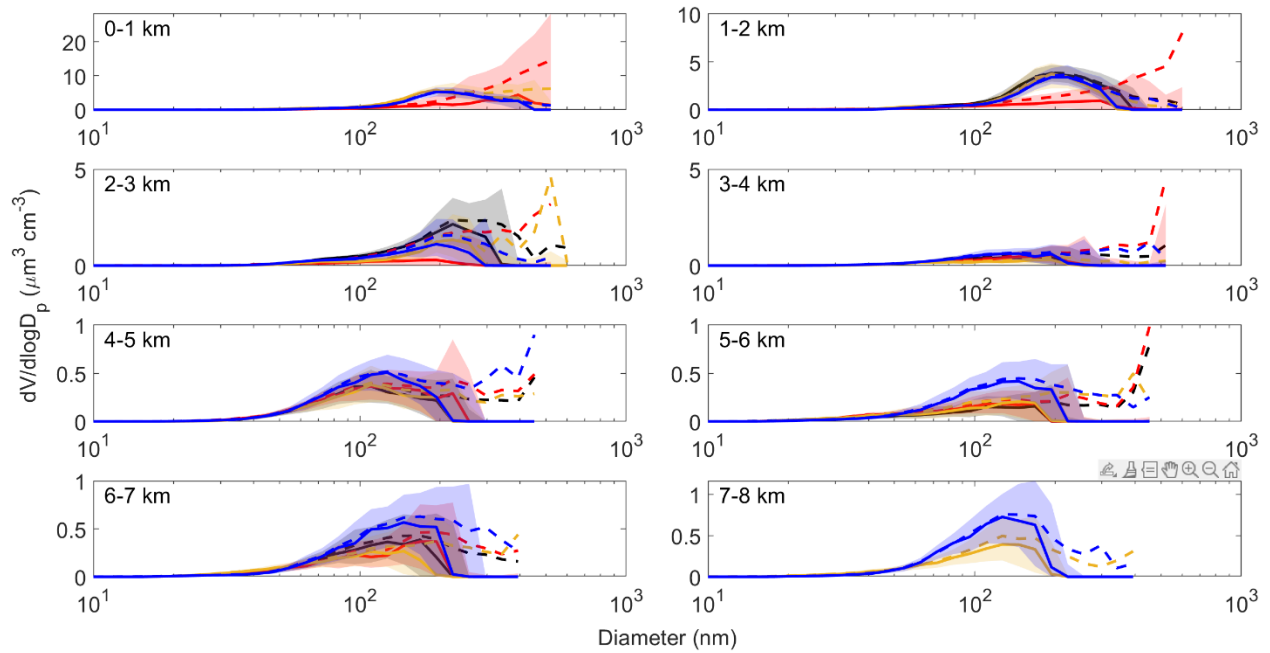
Figure 10. Volume size distributions for the tropical cyclone-induced convection case study. Median (solid line), mean (dashed line), and 25th to 75th percentiles (shaded area) of volume size distributions of submicrometer particles (FIMS) every 1 km altitude on 20 September 2019 from 01:53 to 06:20 UTC. The colors represent four separate vertical profiles, where black was from 01:35 to 02:19 UTC, red was from 03:40 to 04:44 UTC, yellow was from 04:59 to 05:27 UTC, and blue was from 05:52 to 06:20 UTC.

The second case, the shallow cumulus case on 24 September 2019 (Hilario et al., 2025), has multi-level wind trajectories initially from the West Pacific in the northeast direction, which appear to have come from the Philippines and the general southwest direction from two days before (Fig. 9c). The most evident increase in CO (Fig. 9d) is observed between 5-5.5 km, at an altitude lower than the previous case. Both RH and f(RH) have a similar trend to CO throughout the vertical profile, which slightly follows the trend of sulfate mass fraction. This is observed especially in the lower levels (until ~2 km) where RH and f(RH) are relatively steady, even with a large decrease in total aerosol mass.

At higher altitudes, above 4.5 km, f(RH) increases to a greater degree with decreased organic mass fraction and increased sulfate mass fraction (Fig. 9d), possibly due to cloud processing. Like the first case, the VSD plots (Fig. 11) for this case show decreasing VSD magnitudes and volume weighted average diameters with increasing altitudes. The broadening of the VSDs above 3 km, concurrent with the increased decreased sulfate mass fraction, likewise suggests cloud processing. There is a known sulfate source, a power plant in western Luzon, in the Philippines that is along the path of the l.5 km back trajectory (Fig. 9c) and may possibly contribute to sulfate in the region (Lorenzo et al., 2023). It is possible that this and other sulfate sources in the region, such as those from ships (Miller et al., 2023), are being transported vertically and affecting aerosol hygroscopicity in the areas where there is shallow convection.

593
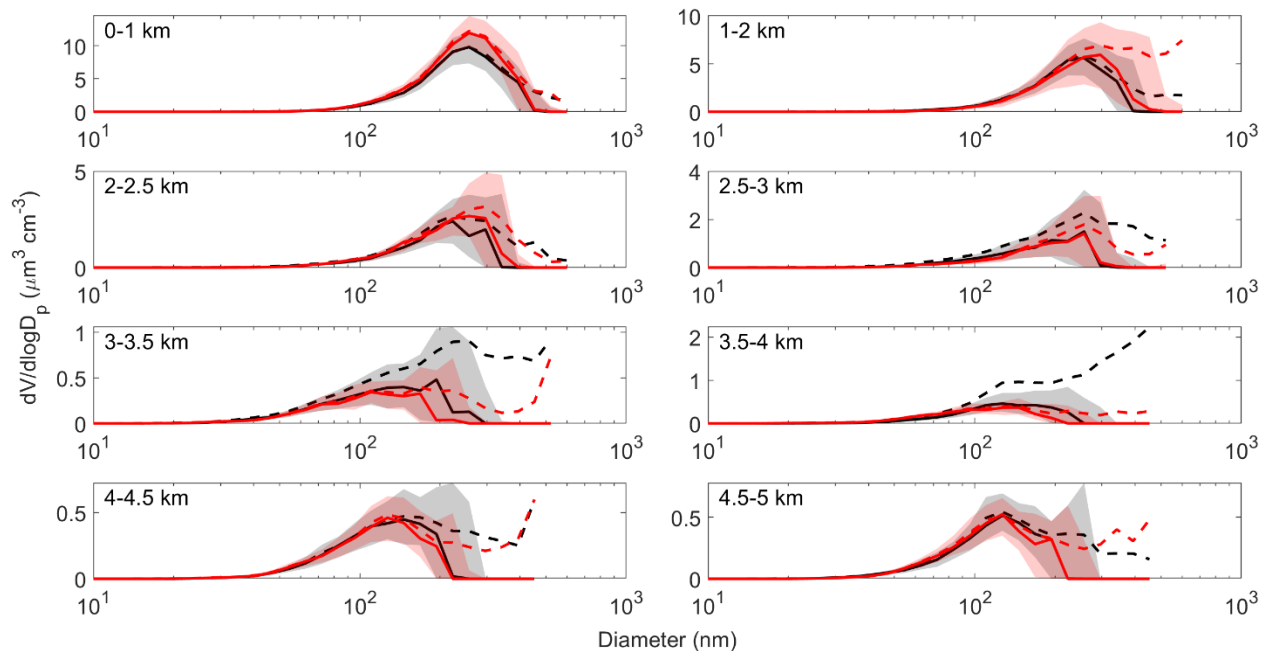
Figure 11. Volume size distributions for the shallow convection case study. Median (solid line), mean (dashed line), and 25th to 75th percentiles (shaded area) of volume size distributions of submicrometer particles (FIMS) in 0.5-1 km altitude increments on 24 September 2019 from 02:55 to 06:02 UTC. The colors represent two separate vertical profiles, where black was from 02:55 to 04:07 UTC and red was from 05:42 to 06:02 UTC.

In summary, for both cases vertical transport in cumulus clouds correspond to higher f(RH) with lower organic mass fractions or increased sulfate mass fractions, at cloud outflow altitudes. At slightly higher altitudes, increasing organics with decreasing ammonium decrease f(RH) for the tropical cyclone case. The VSD magnitudes and the averaged diameter of the aerosol size decrease from cloud base to cloud outflow altitudes, with the VSDs broadening likely due to cloud processing. The understanding and representation of the vertical transport or aerosols due to the tropical cyclone and shallow convection and their role in aerosol-cloud interaction is further investigated as we evaluate modeled data using the two cases that we have just discussed.

3.2.3   Model Evaluation

To give regional context to the cases, we begin the discussion of model evaluation with the horizontal distribution of the modeled (~111 km resolution) near-surface aerosol hygroscopicity (kappa: calculated from the volume fractions and kappa values (Eq. 3) of the modeled submicrometer aerosol species as described in 2.3.2) and winds within the CAMP^{2}Ex domain. We will compare the model kappa values to kappa from different regions around the world based on previous studies. Subsequently, we will discuss how the modeled submicrometer kappa at different vertical levels compare to the kappa derived from bulk f(RH) (< 5 µm) (Eqs. 4 and 5) as well as from kappa derived from submicrometer AMS and SP2 species (Eq. 3) from the aircraft observations.

The CAM-chem modeled surface kappa values (Fig. 12) in the CAMP^{2}Ex region of interest, during the time when the three cases discussed in 3.2.1 and 3.2.2 were sampled, are within the range of globally modeled surface kappa in clean

615 marine (0.9 – 1.0), continental (0.1 – 0.4), and continental outflow / polluted marine (0.4 – 0.6) regions from previous

616 studies (Pringle et al., 2010). The highest modeled kappa (~1.0, Figs. 12a and 12b) is like those previously found in

617 clean marine areas. The high kappa values are influenced by the strong winds, which can increase sea salt emissions,

618 due to the tropical cyclone which was still developing on 16 September 2019 and more fully developed on 20

619 September 2019. The Pacific Ocean also is the source of high kappa (~0.9 - 1.0) for the shallow convection case on

620 24 September 2019 (Fig. 12c). For all three cases there was low kappa (< 0.4) in areas with low wind speeds and over

621 land especially over Borneo and East Asia, typical of continental and continental outflow regions. For the two cases

622 that were within the southwest monsoon (Figs. 13a and 13b) the lowest kappa values (< 0.2) were in Borneo and

623 downwind areas including Southern Philippines and areas east of it.

624 The modeled surface kappa (~0.1 – 0.5) below the aircraft positions for the case studies of interest (pink lines in Fig.

625 12), though over the sea, are lower than in those areas most affected by the Pacific Ocean and are influenced by

626 emissions from Borneo (Figs. 7a and 12a), East Asia (Figs. 9a and 12b) and the Philippines (Fig. 9c and 12c) based

627 on back trajectories. Kappa, calculated from the median f(RH) derived from scattering measurements, for the five air

628 masses discussed in sections 3.1 and 3.2 (MC: -0.02, EA: 0.14, PSEA: 0.10, WP: 0.24, and Other: 0.11), all fall in the

629 continental category even though the majority of these air masses are technically in regions with continental outflow

630 or polluted marine regions. The CAM-chem kappa values for the aircraft positions for the case studies with vertical

631 transport (Figs. 12b and 12c) the CAM-chem kappa values (~0.40 – 0.50) are more than double the range of calculated

632 kappa from East Asia (0.14) and Other (0.11) air masses that are influencing the case studies. To make sense of this

633 difference between globally modeled surface kappa values and that which is calculated from the CAMP²Ex f(RH), we

634 delve more into aerosol vertical transport and its connection to aerosol hygroscopicity and evaluate the vertical profile

635 of the kappa calculated from the CAM-chem model outputs.

636
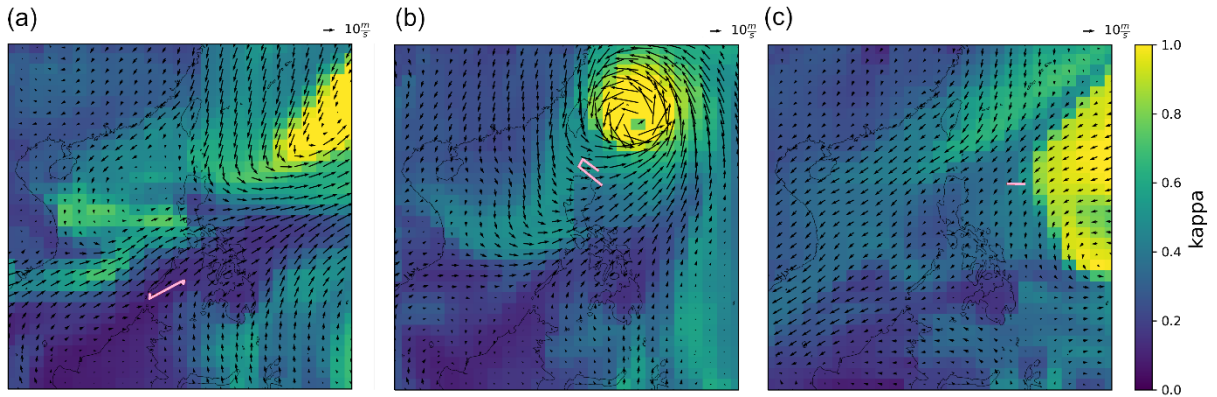
637 **Fig. 12. Modeled kappa and winds at 957 hPa for (a) the biomass burning smoke case at 06:00 UTC on 16 September 2019,**
638 **(b) the tropical cyclone-induced case at 06:00 UTC on 20 September 2019 and, (c) the shallow convection case at 06:00 UTC**
639 **on 24 September 2019. The pink lines represent the aircraft locations from 02:15 to 04:22 UTC on 16 September 2019, 01:53**
640 **to 06:20 UTC on 20 September 2019 and, from 02:55 to 06:02 UTC on 24 September 2019. The approximate aircraft**
641 **locations are represented by pink lines.**

642 The CAM-chem model (Fig. 13a) was able to represent the general trends in the observed total submicrometer mass
643 vertical profile for the tropical cyclone-induced convection case. The observations from AMS are only for non-
644 refractory aerosol species, however, and so sea salt and dust are not included in the total mass, possibly affecting the
645 comparison with the model output, which accounts for both. The uniform ~111 km grid mesh CAM-chem and
646 MUSICA outputs show approximate contributions by sea salt and dust to be 5 to 20 % of the total mass (Figs. 13d
647 and 13e). This could explain the higher total mass values from the model outputs compared to observations for some
648 altitude levels, though in general even without dust and sea salt the CAM-chem model still has slightly higher aerosol
649 total mass values (dashed lines in Fig. 13a) compared to the observations. The CAM-chem model represents the
650 approximate aerosol total mass well for this case probably because of its large-scale nature, where wind speeds were
651 high (> 20 m s^{-1}) and where the aerosol particles are potentially from a large source (East Asia) (Figs. 9a and 13a).
652 Together, the sum of the sulfate and ammonium mass fractions are similar for the observed (Fig. 13c) and modeled
653 outputs close to the surface (Figs. 13d and 13e), where the model output is ammonium bisulfate and not just sulfate,
654 but the actual mass concentrations of sulfate from the models are generally higher than the observations above 1 km
655 (Fig. S1a). This sulfate-based compound dominates the total aerosol mass for both the observations and model outputs,
656 as is expected based on its source air mass from East Asia, and accounts for the similar observed and modeled total
657 mass shape profiles (Fig. S1). The organic mass fraction, on the other hand, is lower by almost half of the observed
658 organic mass fraction due to sulfate dominating. This has a direct effect on modeled aerosol hygroscopicity (kappa),
659 as it was shown earlier that f(RH) decreases with an increased organic mass fraction (Fig. 4).

660
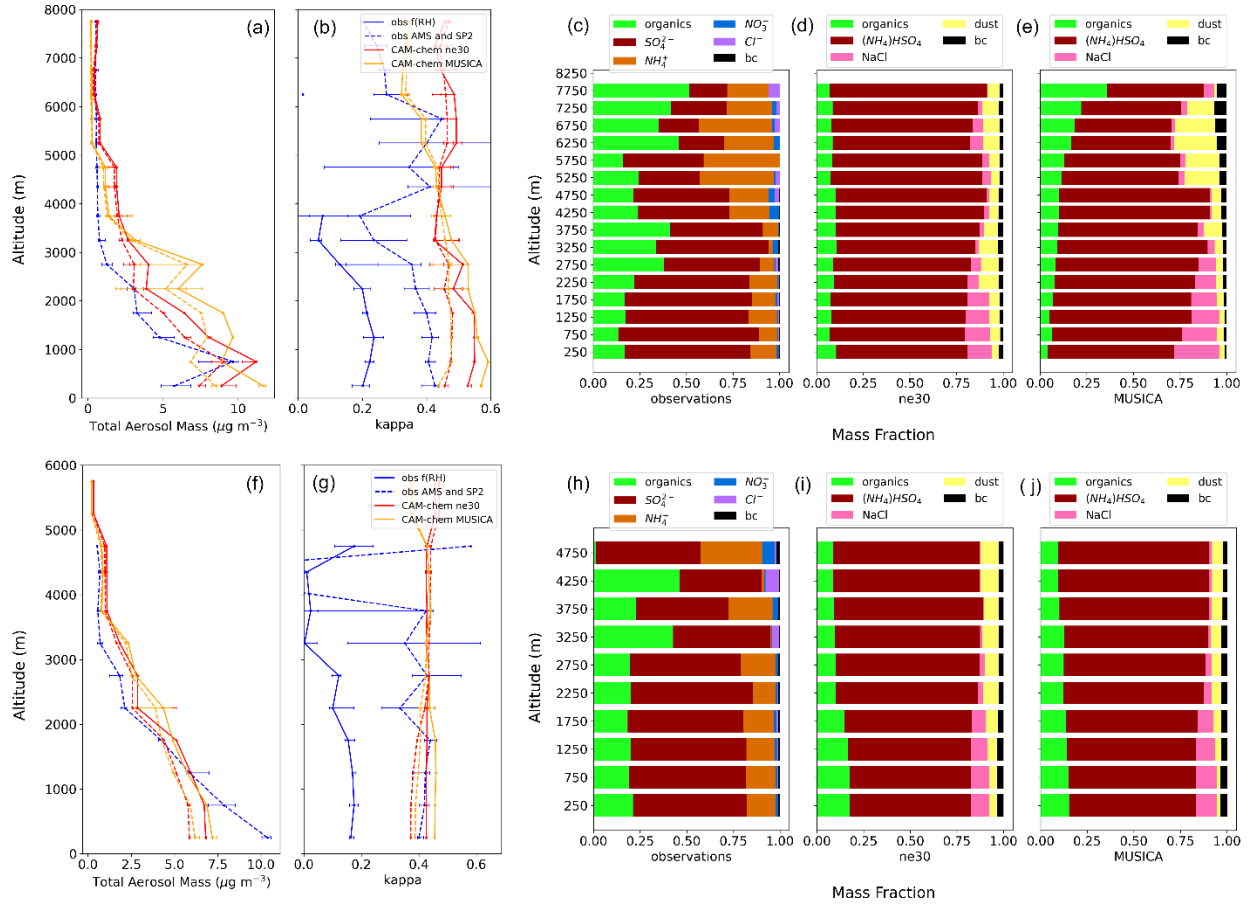
Figure 13. Vertical profiles of observed data and CAM-chem model outputs for ne30 ~1° and MUSICA 0.25° grids for (a-e) the tropical cyclone-induced convection case on 20 September 2019 and (f-j) the shallow convection case on 24 September 2019 at 500 m intervals. (a) Total observed submicrometer aerosol mass (01:53 to 06:20 UTC) from AMS (organics, SO₄²⁻, NO₃⁻, NH₄⁺, Cl⁻) and SP2 (black carbon (BC)) data and CAM-chem output (06:00 UTC) (organics: primary/hydrophobic, hygroscopic, and secondary ($C_{15}H_{38}O_2$), sulfate (NH_4HSO_4), sea salt, dust ($AlSiO_5$), and black carbon (primary/hydrophobic and hygroscopic)) where the solid line includes all the CAM-chem species and the dashed line excludes dust and sea salt and (b) calculated kappa from observed *f*(RH=82 % ± 10 %/RH<40 %) at 550 nm (solid line, < 5 μm) and from AMS and SP2 (dashed line, submicrometer) data and using ZSR mixing rule for all CAM-chem aerosol species (solid line, submicrometer) and excluding dust and sea salt (dashed line). The lines correspond to the median values of data in the given altitude intervals and the bars correspond to the 25ᵗʰ and 75ᵗʰ percentile values. Submicrometer median mass fractions at 500 m intervals of (c) observational data (01:53 to 06:20 UTC) and (d-e) corresponding CAM-chem model outputs (06:00 UTC) for (d) ne30 ~1° and (e) MUSICA 0.25° grids for the tropical cyclone-induced convection case on 20 September 2019. CAM-chem outputs were combined into five main categories: organics (primary/hydrophobic, hygroscopic, and secondary ($C_{15}H_{38}O_2$)); sulfate (NH_4HSO_4); sea salt; dust ($AlSiO_5$); and black carbon (primary/hydrophobic and hygroscopic). (f) Total observed submicrometer aerosol mass (02:55 to 06:02 UTC) from AMS and SP2 data and (06:00 UTC) CAM-chem output and (g) calculated kappa from observed *f*(RH=82 % ± 10 %/RH<40 %) and from AMS and SP2 data. Submicrometer median mass fractions of (h) observational data (02:55 to 06:02 UTC) and (i-j) corresponding CAM-chem model outputs (06:00 UTC) for the shallow convection case on 24 September 2019.

Median modeled kappa for the tropical cyclone-induced convection case is more than twice in magnitude compared to the median derived kappa from *f*(RH) (Fig. 13b), though they have a similar vertical profile shape. It has been noted

683   from previous studies that the conversion of observed f(RH) to kappa (Brock et al., 2016b) may be associated with up

684   to 40 % uncertainty (van Diedenhoven et al., 2022), though this does not change that the kappa from CAM-chem is

685   still approximately twice the calculated observed kappa. We note that additional uncertainties as a result of the

686   conversion from Brock et al. (2016b) could also be contributing to the discrepancy. Brock et al. (2016b) used

687   submicrometer measurements in the southeast U.S. while CAMP^{2}Ex f(RH) was calculated for particles less than 5

688   µm. Kappa calculated from f(RH) represents larger particles (< 5 µm) compared to the kappa calculated from CAM-

689   chem (< 0.48 µm), and the difference in size of the particles could be contributing to this disparity in kappa.

690   We compare more similar sized particles, kappa derived from AMS and SP2 measurements (< 0.70 µm) with kappa

691   calculated from CAM-chem (Fig. 13b), and find that the kappa derived from the AMS and SP2 is still lower than that

692   computed from CAM-chem outputs. The kappa from AMS and SP2 is approximately twice (100 % larger than) the

693   kappa from f(RH), probably due to more than just particle size differences. Based on Mie theory and studies comparing

694   f(RH) of PM_1 and PM_{10} particles (Zieger et al., 2013; Titos et al., 2021), CAMP^{2}Ex f(RH) would be larger if it were

695   measuring just submicrometer particles due to the increased scattering efficiency for accumulation mode particles

696   compared to coarse particles. Though, based on Fig. 3 of Titos et al. (2021), the difference in f(RH) in marine sites

697   would only be ~0.1 (given median observed SAE) and that would translate to ~20 to 40 % increase in kappa. Thus,

698   although size plays a role, composition is also contributing to the difference in the calculated kappa values between

699   observations and the model. Examples of past studies in the region with low kappa values suggest that both the size

700   and compositional effect together are important. Lab experiments of tropical peat burning showed that smaller (70

701   nm) primary organic particles (POA) became more oxidized faster compared to larger particles (150 nm) and kappa

702   for oxidized POA (100 nm) was 0.16 (Chen et al., 2022). Ground measurements of aerosol particles (56 nm – 100 nm)

703   in Quezon City in the Philippines, which were dominated by elemental carbon, yielded kappa values less than 0.10

704   (AzadiAghdam et al., 2019).

705   The over and under-represented mass of sulfates and organics, respectively (Fig. 13b), by the model may be causing

706   the higher kappa in the model. Based on the discussion in section 3.1.2 on air masses coming from East Asia (Fig.

707   4c), as is the case for this event, an organic mass fraction that is lower by half can increase the f(RH) (f(RH = (-0.81

708   * organic mass fraction) + 1.56) and therefore the derived kappa by ~70 %. Organics, especially secondary organic

709   aerosols have been underpredicted by CAM-chem in urban and urban outflow regions (Schwantes et al., 2022). This

710   is consistent with the observations for this case, which is influenced by urban outflow from East Asia and thus affecting

711   the calculated kappa from the model. CO (Fig. S1) is also underrepresented by the model potentially due to emissions

712   inventories (Hua et al., 2024).

713   For the case of shallow convection, the shape of the vertical profile of the CAM-chem model output total mass

714   concentration is similar to the observed total mass concentration profile (Fig. 13f), though it underestimates the

715   observed total concentration by approximately 2 to 4.5 µg m^{-3} below 1 km altitude, and then overestimates

716   concentrations by approximately 0.5 to 2 µg m^{-3} above 1 km. This is due to the model underestimating organics and

717   sulfate close to the surface, while sulfate is overestimated above 1 km (Fig. S1b). The effect of this is seen in the

model-derived kappa, which is, like the previous case, higher than the calculated kappa from observations, though to a lesser degree (Fig. 13g). Unlike the case of the tropical cyclone-induced convection, the modeled kappa is relatively unchanging in shape compared to the kappa derived from observations. This is likely due to the differences in the compositional profile at the higher altitudes, even if the total mass is similar. The model is not able to represent the increase and decrease in organic mass fraction from 3.5 to 4.5 km (Fig. 13h) and dominance of sulfate above 4.5 km. At those altitudes the observations become dominated by sulfate, ammonium, and nitrate (Fig. 13h), even with losses due to scavenging and activation as shown by decreased aerosol mass with altitude, probably due to the in-cloud production of sulfate as discussed in section 3.2.2. The mass fraction profiles from the model (Figs. 13i and 13j) appear to have a steadily decreasing (increasing) organic and sea salt (sulfate and dust) mass fraction with height. This case is a smaller scale event with smaller surface winds associated with it (Fig. 12b) compared to the tropical cyclone case. With weak forcing, it is likely that the CAM cumulus parameterizations does not predict the convection observed in the shallow convection case affecting modeled aerosol mass vertical distribution and, consequently, kappa in both the uniform ~111 global model and the regionally refined simulations. This is similar to a model evaluation study (i.e. GEOS and GOCART) of CAMP^{2}Ex aerosol extinction data, which recommended an improvement of shallow convection schemes to improve the representation of vertical transport (Collow et al., 2022). In fact, the CO increase above 5 km, that that we used to identify convection, is not captured by CAM-chem (Fig. S2). What is consistent though is that for both the observations and model output of this shallow convection case, the relative magnitude of the model kappa is lower than that of the tropical cyclone case.

4. Conclusion

This study reports on low PM$_5$ (D$_p$ < 5 μm) aerosol hygroscopicity measured during CAMP^{2}Ex 2019 in Southeast Asia due to organics from biomass burning. Aging and vertical transport changes the hygroscopicity of particles affecting clouds in the region. Comparisons with a global atmospheric chemistry model reveal discrepancies between observed and modeled aerosol concentrations and hygroscopicity, emphasizing the need to improve emissions inventories and shallow cloud parameterizations. Notable results of this work, following the study goals raised at the end of Section 1 are as follows:

The generally low median f(RH) (1.24 with Q1 and Q3 of 1.05 and 1.43, respectively) of aerosol particles (< 5 μm) in Southeast Asia during the CAMP^{2}Ex campaign from 24 August to 5 October in 2019 is linked to the dominating regional effect of biomass burning from the Maritime Continent. Measurements of f(RH) in other polluted marine environments around the world for PM$_{10}$ (< 10 μm) and PM$_1$ (< 1 μm) particles have higher ranges (median of ~1.7 – 2.0) of f(RH) values (Titos et al., 2021). The median f(RH) of air masses from the Maritime Continent was exceptionally low (1.05 with Q1 and Q3 of 0.94 and 1.20, respectively) for polluted marine environments and are more similar to those with biomass burning (Gomez et al., 2018). The air masses with the highest f(RH) from CAMP^{2}Ex are generally from the West Pacific, in the northernmost regions of the Philippines and farthest away from the Maritime Continent. Their median f(RH) (1.49 with Q1 and Q3 of 1.26 and 1.73, respectively) is also lower than what has been associated with typical polluted marine environments.

753 Throughout CAMP²Ex, submicrometer organic matter is the main aerosol component associated with biomass burning
754 and the low f(RH) values. Organics are a major feature of total aerosol mass, especially in air masses traced back to
755 the Maritime Continent. Biomass burning smoke is spread out in the region increasing AOD downwind of the MC
756 (Fig. 2 in Reid et al. (2023)) and is corroborated by cases of sub-1 f(RH) and submicrometer reflective particles with
757 elevated organic mass fractions that are present in all the air masses. Based on clustering analysis using optical
758 properties, majority of the particles sampled during the campaign appear to be a mixture of both organic and elemental
759 carbon. Organics dominate in terms of mass fraction due to the smoldering-type burning in peat fire (Reid et al., 2023)
760 from the Maritime Continent, which is known to produce more organics than elemental carbon (Reid et al., 2005).
761 This is consistent with what Miller et al. (2023) observed where the highest median levels of organic and elemental
762 carbon mass during CAMP²Ex were due to biomass burning from the Maritime Continent. Without organics, the
763 baseline f(RH) (1.38 – 1.55, Fig. 4), is still lower than measurements from other areas (i.e. ~1.8 from the Yangtze
764 River Delta in China and from INDOEX over the Indian Ocean, 2.19 from SEAC⁴RS in and around the U.S., ~2.6
765 from ICARTT over North America and Europe, ~3 from ACE-ASIA over the Yellow Sea and Sea of Japan, and ~3.5
766 from Melpitz, Germany) (Zhang et al., 2015; Quinn et al., 2005; Shingler et al., 2016a; Zieger et al., 2014) probably
767 due to the presence of elemental carbon, which is the second most dominant aerosol type during the campaign. The
768 unique relationship between organic matter and hygroscopicity in the CAMP²Ex region is important information that
769 can help in model evaluations (Burgos et al., 2020).

770 Farther away from the Maritime Continent, the organic particles have aged and become more oxidized as they
771 interacted with the other air masses. The West Pacific is a remote region in northern Philippines and is downwind of
772 biomass burning from MC, resulting in a combined marine and polluted aerosol. The oldest biomass burning aerosols
773 were observed there. The organic oxidation values of the aerosol particles in the air mass from the West Pacific are
774 close to the threshold of maximum oxidation that has been observed in previous studies (Cubison et al., 2011). Vertical
775 transport decreases and increases hygroscopicity at cloud level with increased organic and sulfate mass fractions,
776 respectively, in the West Pacific. These aerosol constituents are thought to be transported from the MC and the
777 Philippines and their surrounding oceans, where natural and industrial sources are significant (Miller et al., 2023), and
778 then cloud processed.

779 Evaluation of the global chemical transport CAM-chem model at two output grids (~111 km and 25 km) against two
780 convective cases from CAMP²Ex show the underrepresentation of organics in general and a higher derived aerosol
781 hygroscopicity (kappa), which may be linked to the possible overestimation of aerosol hygroscopicity from biomass
782 burning based on studies of aerosol optical depth and extinction in the area (Collow et al., 2022; Edwards et al., 2022).
783 CAM-chem overestimates sulfate in the tropical cyclone induced convection case, consistent with results from an
784 assessment of the NAAPS reanalysis product on the positive bias of sulfate from East Asia (Edwards et al., 2022).
785 The vertical representation of the aerosol composition for the larger scale convection case due to a tropical cyclone is
786 better than that for the shallow convection case. Cloud processing and increased hygroscopicity are not captured by
787 the model for the shallow convection case, irrespective of model grid size. The representation of shallow convection
788 in the area by global models remains challenging, based on other model-evaluation studies (Collow et al., 2022). Past

studies on biomass burning aerosol effects on convection in Southeast Asia using a cloud-scale model emphasized the importance of aerosol composition and absorptive properties, and their effect on atmospheric stability, in the understanding of aerosol-cloud interactions (Hodzic and Duvel, 2018). It is thus ideal that cloud-scale models be evaluated using the dataset from CAMP²Ex, where the invigoration of shallow clouds has been observed (Reid et al., 2023).

The implications of the low aerosol hygroscopicity in the region and its effects on clouds and climate are just beginning to be unraveled. The mixing and aging of organic and elemental carbon from biomass burning smoke in the Maritime Continent with background and transported sources influences hygroscopicity observations and modeling uncertainties and can be the topic of future work. Improvements in harmonization in terms of aerosol particle sizes and composition, along with updated emissions inventories, will be helpful moving forward both for the observations and modeling of aerosol hygroscopicity. These suggestions can hopefully improve shallow cumulus representation, which is still the biggest source of differences in model sensitivity in the understanding of climate change (Bony and Dufresne, 2005), in the region and globally. Emerging endeavors to implement higher resolution schemes in a large domain (Pfister et al., 2020; Radtke et al., 2021) to capture both fine scale aerosol-cloud processes along with improved observations in Southeast Asia hold promise.

Data availability. CAMP²Ex data archived per research flight and parameter type can be found at:
https://doi.org/10.5067/Airborne/CAMP2Ex_Aerosol_AircraftInSitu_P3_Data_1 (P-3 In-Situ Aerosol Data),
https://doi.org/10.5067/Airborne/CAMP2Ex_Cloud_AircraftInSitu_P3_Data_1 (P-3 In-Situ Cloud Data),
https://doi.org/10.5067/Airborne/CAMP2Ex_MetNav_AircraftInSitu_P3_Data_1 (P-3 In-Situ Meteorological and Navigational Data), and https://doi.org/10.5067/Airborne/CAMP2Ex_TraceGas_AircraftInSitu_P3_Data_1 (P-3 In-Situ Trace Gas Data). CAM-chem model outputs can be found at https://doi.org/10.6084/m9.figshare.26755936.v1.

Author contributions. LDZ, ECC, JPDG, GSD, RF, MRAH, MS, JW, QX, and AS carried out various aspects of the data collection. ST and JZ conducted the CAM-chem model simulations. GRL, LDZ, AFA, MB, ECC, RF, MRAH, MS, JW, QX, and AS performed analysis and interpretation of the data. GRL and AS prepared the manuscript with contributions from the coauthors.

Competing interests. At least one of the (co-)authors is a member of the editorial board of *Atmospheric Chemistry and Physics.*

Special issue statement. This article is part of the special issue "Cloud Aerosol and Monsoon Processes Philippines Experiment (CAMP²Ex) (ACP/AMT inter-journal SI)". It is not associated with a conference.

823 *Acknowledgements.* The authors gratefully acknowledge the NOAA Air Resources Laboratory (ARL) for the

824 provision of the HYSPLIT transport and dispersion model and READY website (https://www.ready.noaa.gov) used

825 in this publication. The NSF National Center for Atmospheric Research is a major facility sponsored by the U.S.

826 National Science Foundation under Cooperative Agreement No. 1852977.

827

828 *Financial support.* This research has been supported by the National Aeronautics and Space Administration (grant

829 no. 80NSSC18K0148) and ONR grant N00014-21-1-2115.

830

References

832 Adam, M. G., Tran, P. T., Bolan, N., and Balasubramanian, R.: Biomass burning-derived
833 airborne particulate matter in Southeast Asia: A critical review, Journal of Hazardous Materials,
834 407, 124760, https://doi.org/10.1016/j.jhazmat.2020.124760, 2021.
835 Amnuaylojaroen, T.: Air Pollution Modeling in Southeast Asia—An Overview, Vegetation Fires
836 and Pollution in Asia, 531-544, https://doi.org/10.1007/978-3-031-29916-2_31, 2023.
837 Anderson, T. L., and Ogren, J. A.: Determining aerosol radiative properties using the TSI 3563
838 integrating nephelometer, Aerosol Science and Technology, 29, 57-69,
839 https://doi.org/10.1080/02786829808965551, 1998.
840 Ångström, A.: On the atmospheric transmission of sun radiation and on dust in the air,
841 Geografiska Annaler, 11, 156-166, https://doi.org/10.1080/20014422.1929.11880498, 1929.
842 Attwood, A., Washenfelder, R., Brock, C., Hu, W., Baumann, K., Campuzano-Jost, P., Day, D.,
843 Edgerton, E., Murphy, D., and Palm, B.: Trends in sulfate and organic aerosol mass in the
844 Southeast US: Impact on aerosol optical depth and radiative forcing, Geophysical Research
845 Letters, 41, 7701-7709, https://doi.org/10.1002/2014GL061669, 2014.
846 AzadiAghdam, M., Braun, R. A., Edwards, E.-L., Bañaga, P. A., Cruz, M. T., Betito, G.,
847 Cambaliza, M. O., Dadashazar, H., Lorenzo, G. R., and Ma, L.: On the nature of sea salt aerosol
848 at a coastal megacity: Insights from Manila, Philippines in Southeast Asia, Atmos. Environ., 216,
849 116922, https://doi.org/10.1016/j.atmosenv.2019.116922, 2019.
850 Barth, M., Rasch, P., Kiehl, J., Benkovitz, C., and Schwartz, S.: Sulfur chemistry in the National
851 Center for Atmospheric Research Community Climate Model: Description, evaluation, features,
852 and sensitivity to aqueous chemistry, J. Geophys. Res.- Atmos., 105, 1387-1415,
853 https://doi.org/10.1029/1999JD900773, 2000.
854 Baynard, T., Garland, R., Ravishankara, A., Tolbert, M., and Lovejoy, E.: Key factors
855 influencing the relative humidity dependence of aerosol light scattering, Geophysical research
856 letters, 33, https://doi.org/10.1029/2005GL024898, 2006.
857 Bergstrom, R. W., Pilewskie, P., Russell, P. B., Redemann, J., Bond, T. C., Quinn, P. K., and
858 Sierau, B.: Spectral absorption properties of atmospheric aerosols, Atmos. Chem. Phys., 7, 5937-
859 5943, https://doi.org/10.5194/acp-7-5937-2007, 2007.
860 Bony, S., and Dufresne, J. L.: Marine boundary layer clouds at the heart of tropical cloud
861 feedback uncertainties in climate models, Geophysical Research Letters, 32,
862 https://doi.org/10.1029/2005GL023851, 2005.

863   Brock, C., Wagner, N., and Gordon, T.: Effect of Aerosol Size and Hygroscopicity on Aerosol
864   Optical Depth in the Southeastern United States, EGU General Assembly Conference Abstracts,
865   2016a.
866   Brock, C. A., Wagner, N. L., Anderson, B. E., Attwood, A. R., Beyersdorf, A., Campuzano-Jost,
867   P., Carlton, A. G., Day, D. A., Diskin, G. S., and Gordon, T. D.: Aerosol optical properties in the
868   southeastern United States in summer-Part 1: Hygroscopic growth, https://doi.org/10.5194/acp-
869   16-4987-2016, 2016b.
870   Brooks, S. D., Wise, M. E., Cushing, M., and Tolbert, M. A.: Deliquescence behavior of
871   organic/ammonium sulfate aerosol, Geophysical Research Letters, 29, 23-21-23-24,
872   https://doi.org/10.1029/2002GL014733, 2002.
873   Burgos, M. A., Andrews, E., Titos, G., Alados-Arboledas, L., Baltensperger, U., Day, D.,
874   Jefferson, A., Kalivitis, N., Mihalopoulos, N., and Sherman, J.: A global view on the effect of
875   water uptake on aerosol particle light scattering, Scientific data, 6, 1-19,
876   https://doi.org/10.1038/s41597-019-0158-7, 2019.
877   Burgos, M. A., Andrews, E., Titos, G., Benedetti, A., Bian, H., Buchard, V., Curci, G., Kipling,
878   Z., Kirkevåg, A., and Kokkola, H.: A global model–measurement evaluation of particle light
879   scattering coefficients at elevated relative humidity, Atmospheric Chemistry and Physics, 20,
880   10231-10258, https://doi.org/10.5194/acp-20-10231-2020, 2020.
881   Cazorla, A., Bahadur, R., Suski, K., Cahill, J. F., Chand, D., Schmid, B., Ramanathan, V., and
882   Prather, K.: Relating aerosol absorption due to soot, organic carbon, and dust to emission sources
883   determined from in-situ chemical measurements, Atmospheric Chemistry and Physics, 13, 9337-
884   9350, https://doi.org/10.5194/acp-13-9337-2013, 2013.
885   Chandra, A. S., Zhang, C., Klein, S. A., and Ma, H. Y.: Low-cloud characteristics over the
886   tropical western Pacific from ARM observations and CAM5 simulations, Journal of Geophysical
887   Research: Atmospheres, 120, 8953-8970, https://doi.org/10.1002/2015JD023369, 2015.
888   Che, H., Segal-Rozenhaimer, M., Zhang, L., Dang, C., Zuidema, P., Dobracki, A., Sedlacek III,
889   A. J., Coe, H., Wu, H., and Taylor, J.: Cloud processing and weeklong ageing affect biomass
890   burning aerosol properties over the south-eastern Atlantic, Communications earth &
891   environment, 3, 182, https://doi.org/10.1038/s43247-022-00517-3, 2022.
892   Chen, J., Zhao, C., Ma, N., and Yan, P.: Aerosol hygroscopicity parameter derived from the light
893   scattering enhancement factor measurements in the North China Plain, Atmospheric Chemistry
894   and Physics, 14, 8105-8118, https://doi.org/10.5194/acp-14-8105-2014, 2014.
895   Chen, J., Budisulistiorini, S. H., Itoh, M., and Kuwata, M.: Roles of relative humidity and
896   particle size on chemical aging of tropical peatland burning particles: Potential influence of
897   phase state and implications for hygroscopic property, Journal of Geophysical Research:
898   Atmospheres, 127, e2022JD036871, https://doi.org/10.5194/acp-22-13219-2022, 2022.
899   Chen, Q., McGowan, S., Gouramanis, C., Fong, L., Balasubramanian, R., and Taylor, D.:
900   Rapidly rising transboundary atmospheric pollution from industrial and urban sources in
901   Southeast Asia and its implications for regional sustainable development, Environ. Res. Lett., 15,
902   1040a1045, https://doi.org/10.1088/1748-9326/abb5ce, 2020.
903   Collow, A. B. M., Buchard, V., Colarco, P. R., da Silva, A. M., Govindaraju, R., Nowottnick, E.
904   P., Burton, S., Ferrare, R., Hostetler, C., and Ziemba, L.: An evaluation of biomass burning
905   aerosol mass, extinction, and size distribution in GEOS using observations from CAMP 2 Ex,
906   Atmospheric Chemistry and Physics, 22, 16091-16109, https://doi.org/10.5194/acp-22-16091-
907   2022, 2022.

Covert, D. S., Charlson, R., and Ahlquist, N.: A study of the relationship of chemical composition and humidity to light scattering by aerosols, Journal of Applied Meteorology, 11, 968-976, https://doi.org/10.1175/1520-0450(1972)011<0968:ASOTRO>2.0.CO;2, 1972.

Crosbie, E., Ziemba, L. D., Shook, M. A., Robinson, C. E., Winstead, E. L., Thornhill, K. L., Braun, R. A., MacDonald, A. B., Stahl, C., and Sorooshian, A.: Measurement report: Closure analysis of aerosol–cloud composition in tropical maritime warm convection, Atmos. Chem. Phys., 22, 13269-13302, https://doi.org/10.5194/acp-22-13269-2022, 2022.

Crumeyrolle, S., Gomes, L., Tulet, P., Matsuki, A., Schwarzenboeck, A., and Crahan, K.: Increase of the aerosol hygroscopicity by cloud processing in a mesoscale convective system: a case study from the AMMA campaign, Atmospheric Chemistry and Physics, 8, 6907-6924, https://doi.org/10.5194/acp-8-6907-2008, 2008.

Cruz, M. T., Bañaga, P. A., Betito, G., Braun, R. A., Stahl, C., Aghdam, M. A., Cambaliza, M. O., Dadashazar, H., Hilario, M. R., Lorenzo, G. R., Ma, L., MacDonald, A. B., Pabroa, C., Yee, J. R., Simpas, J. B., and Sorooshian, A.: Size-resolved composition and morphology of particulate matter during the southwest monsoon in Metro Manila, Philippines, Atmos. Chem. Phys., 19, 10675–10696, https://doi.org/10.5194/acp-19-10675-2019, 2019.

Cubison, M., Ortega, A., Hayes, P., Farmer, D., Day, D., Lechner, M., Brune, W., Apel, E., Diskin, G., and Fisher, J.: Effects of aging on organic aerosol from open biomass burning smoke in aircraft and laboratory studies, Atmospheric Chemistry and Physics, 11, 12049-12064, https://doi.org/10.5194/acp-11-12049-2011, 2011.

Dadashazar, H., Corral, A. F., Crosbie, E., Dmitrovic, S., Kirschler, S., McCauley, K., Moore, R., Robinson, C., Schlosser, J. S., and Shook, M.: Organic enrichment in droplet residual particles relative to out of cloud over the northwestern Atlantic: analysis of airborne ACTIVATE data, Atmospheric Chemistry and Physics, 22, 13897-13913, https://doi.org/10.5194/acp-22-13897-2022, 2022.

Delene, D. J., and Ogren, J. A.: Variability of aerosol optical properties at four North American surface monitoring sites, Journal of the Atmospheric Sciences, 59, 1135-1150, https://doi.org/10.1175/1520-0469(2002)059<1135:VOAOPA>2.0.CO;2, 2002.

Dockery, D. W.: Epidemiologic evidence of cardiovascular effects of particulate air pollution, Environmental health perspectives, 109, 483-486, https://doi.org/10.1289/ehp.01109s4483, 2001.

Doherty, S. J., Quinn, P. K., Jefferson, A., Carrico, C. M., Anderson, T. L., and Hegg, D.: A comparison and summary of aerosol optical properties as observed in situ from aircraft, ship, and land during ACE-Asia, Journal of Geophysical Research: Atmospheres, 110, https://doi.org/10.1029/2004JD004964, 2005.

Dong, X., Fu, J. S., Huang, K., Lin, N.-H., Wang, S.-H., and Yang, C.-E.: Analysis of the co-existence of long-range transport biomass burning and dust in the subtropical West Pacific Region, Scientific Reports, 8, 8962, https://doi.org/10.1038/s41598-018-27129-2, 2018.

Dubovik, O., Holben, B., Eck, T. F., Smirnov, A., Kaufman, Y. J., King, M. D., Tanré, D., and Slutsker, I.: Variability of absorption and optical properties of key aerosol types observed in worldwide locations, J. Atmos. Sci., 59, 590-608, https://doi.org/10.1175/1520-0469(2002)059<0590:VOAAOP>2.0.CO;2, 2002.

Dumka, U., Kaskaoutis, D., Sagar, R., Chen, J., Singh, N., and Tiwari, S.: First results from light scattering enhancement factor over central Indian Himalayas during GVAX campaign, Science of the Total Environment, 605, 124-138, https://doi.org/10.1016/j.scitotenv.2017.06.138, 2017.

Duplissy, J., DeCarlo, P. F., Dommen, J., Alfarra, M. R., Metzger, A., Barmpadimos, I., Prevot, A. S., Weingartner, E., Tritscher, T., and Gysel, M.: Relating hygroscopicity and composition of

organic aerosol particulate matter, Atmospheric Chemistry and Physics, 11, 1155-1165, https://doi.org/10.5194/acp-11-1155-2011, 2011.

Eck, T. F., Holben, B. N., Reid, J., Giles, D., Rivas, M., Singh, R. P., Tripathi, S., Bruegge, C., Platnick, S., and Arnold, G.: Fog-and cloud-induced aerosol modification observed by the Aerosol Robotic Network (AERONET), J. Geophys. Res.- Atmos., 117, https://doi.org/10.1029/2011JD016839, 2012.

Edwards, E.-L., Reid, J. S., Xian, P., Burton, S. P., Cook, A. L., Crosbie, E. C., Fenn, M. A., Ferrare, R. A., Freeman, S. W., and Hair, J. W.: Assessment of NAAPS-RA performance in Maritime Southeast Asia during CAMP 2 Ex, Atmospheric Chemistry and Physics, 22, 12961-12983, https://doi.org/10.5194/acp-22-12961-2022, 2022.

Eldering, A., Ogren, J., Chowdhury, Z., Hughes, L. S., and Cass, G. R.: Aerosol optical properties during INDOEX based on measured aerosol particle size and composition, Journal of Geophysical Research: Atmospheres, 107, INX2 33-31-INX32 33-38, https://doi.org/10.1029/2001JD001572, 2002.

Engelhart, G., Asa-Awuku, A., Nenes, A., and Pandis, S.: CCN activity and droplet growth kinetics of fresh and aged monoterpene secondary organic aerosol, Atmospheric Chemistry and Physics, 8, 3937-3949, https://doi.org/10.5194/acp-8-3937-2008, 2008.

Faloona, I.: Sulfur processing in the marine atmospheric boundary layer: A review and critical assessment of modeling uncertainties, Atmos. Environ., 43, 2841-2854, https://doi.org/10.1016/j.atmosenv.2009.02.043, 2009.

Fan, X., Liu, J., Zhang, F., Chen, L., Collins, D., Xu, W., Jin, X., Ren, J., Wang, Y., and Wu, H.: Contrasting size-resolved hygroscopicity of fine particles derived by HTDMA and HR-ToF-AMS measurements between summer and winter in Beijing: the impacts of aerosol aging and local emissions, Atmospheric Chemistry and Physics, 20, 915-929, https://doi.org/10.5194/acp-20-915-2020, 2020.

Ferrare, R., Melfi, S., Whiteman, D., Evans, K., Poellot, M., and Kaufman, Y.: Raman lidar measurements of aerosol extinction and backscattering: 2. Derivation of aerosol real refractive index, single-scattering albedo, and humidification factor using Raman lidar and aircraft size distribution measurements, Journal of Geophysical Research: Atmospheres, 103, 19673-19689, https://doi.org/10.1029/98JD01647, 1998.

Ferrare, R., Hair, J., Hostetler, C., Shingler, T., Burton, S. P., Fenn, M., Clayton, M., Scarino, A. J., Harper, D., and Seaman, S.: Airborne HSRL-2 measurements of elevated aerosol depolarization associated with non-spherical sea salt, Frontiers in Remote Sensing, 4, 1143944, https://doi.org/10.3389/frsen.2023.1143944, 2023.

Garland, R. M., Ravishankara, A., Lovejoy, E. R., Tolbert, M. A., and Baynard, T.: Parameterization for the relative humidity dependence of light extinction: Organic-ammonium sulfate aerosol, Journal of Geophysical Research: Atmospheres, 112, https://doi.org/10.1029/2006JD008179, 2007.

Garofalo, L. A., Pothier, M. A., Levin, E. J., Campos, T., Kreidenweis, S. M., and Farmer, D. K.: Emission and evolution of submicron organic aerosol in smoke from wildfires in the western United States, ACS Earth and Space Chemistry, 3, 1237-1247, https://doi.org/10.1021/acsearthspacechem.9b00125, 2019.

Gasparini, R., Collins, D. R., Andrews, E., Sheridan, P. J., Ogren, J. A., and Hudson, J. G.: Coupling aerosol size distributions and size-resolved hygroscopicity to predict humidity-dependent optical properties and cloud condensation nuclei spectra, Journal of Geophysical Research: Atmospheres, 111, https://doi.org/10.1029/2005JD006092, 2006.

Gogoi, M. M., Babu, S. S., Jayachandran, V., Moorthy, K. K., Satheesh, S., Naja, M., and Kotamarthi, V.: Optical properties and CCN activity of aerosols in a high-altitude Himalayan environment: Results from RAWEX-GVAX, Journal of Geophysical Research: Atmospheres, 120, 2453-2469, https://doi.org/10.1002/2014JD022966, 2015.

Gomez, S. L., Carrico, C., Allen, C., Lam, J., Dabli, S., Sullivan, A., Aiken, A. C., Rahn, T., Romonosky, D., and Chylek, P.: Southwestern US biomass burning smoke hygroscopicity: The role of plant phenology, chemical composition, and combustion properties, Journal of Geophysical Research: Atmospheres, 123, 5416-5432, https://doi.org/10.1029/2017JD028162, 2018.

Hänel, G.: The properties of atmospheric aerosol particles as functions of the relative humidity at thermodynamic equilibrium with the surrounding moist air, in: Advances in geophysics, Elsevier, 73-188, 1976.

Hegg, D., Larson, T., and Yuen, P. F.: A theoretical study of the effect of relative humidity on light scattering by tropospheric aerosols, Journal of Geophysical Research: Atmospheres, 98, 18435-18439, https://doi.org/10.1029/93JD01928, 1993.

Hilario, M. R. A., Crosbie, E., Shook, M., Reid, J. S., Cambaliza, M. O. L., Simpas, J. B. B., Ziemba, L., DiGangi, J. P., Diskin, G. S., and Nguyen, P.: Measurement report: Long-range transport patterns into the tropical northwest Pacific during the CAMP 2 Ex aircraft campaign: chemical composition, size distributions, and the impact of convection, Atmos. Chem. Phys., 21, 3777-3802, https://doi.org/10.5194/acp-21-3777-2021, 2021.

Hilario, M. R. A., Barth, M., Bennett, R., Crosbie, E., DiGangi, J. P., Diskin, G. S., Lorenzo, G. R., Rutledge, S., Martin, M. Y., and Ziemba, L.: Quantifying scavenging efficiencies of different aerosol species and size-resolved volume concentrations in tropical convective clouds over the West Pacific, Journal of the Atmospheric Sciences, 82, 267-282, https://doi.org/10.1175/JAS-D-24-0064.1, 2025.

Hodzic, A., and Duvel, J. P.: Impact of biomass burning aerosols on the diurnal cycle of convective clouds and precipitation over a tropical island, Journal of Geophysical Research: Atmospheres, 123, 1017-1036, https://doi.org/10.1002/2017JD027521, 2018.

Hong, Y., and Di Girolamo, L.: Cloud phase characteristics over Southeast Asia from A-Train satellite observations, Atmos. Chem. Phys., 20, 8267-8291, https://doi.org/10.5194/acp-20-8267-2020, 2020.

Höpner, F., Bender, F. M., Ekman, A. M., Andersson, A., Gustafsson, Ö., and Leck, C.: Investigation of two optical methods for aerosol-type classification extended to a Northern Indian Ocean site, Journal of Geophysical Research: Atmospheres, 124, 8743-8763, https://doi.org/10.1029/2018JD029685, 2019.

Hua, W., Lou, S., Huang, X., Xue, L., Ding, K., Wang, Z., and Ding, A.: Diagnosing uncertainties in global biomass burning emission inventories and their impact on modeled air pollutants, Atmospheric Chemistry and Physics, 24, 6787-6807, https://doi.org/10.5194/acp-24-6787-2024, 2024.

Kalberer, M.: Aerosol physics and chemistry, Encyclopedia of Atmospheric Sciences, 1, 23, 2014.

Kar, J., Bremer, H., Drummond, J. R., Rochon, Y. J., Jones, D. B., Nichitiu, F., Zou, J., Liu, J., Gille, J. C., and Edwards, D. P.: Evidence of vertical transport of carbon monoxide from Measurements of Pollution in the Troposphere (MOPITT), Geophysical research letters, 31, 2004.

Kavouras, I. G., Nikolich, G., Etyemezian, V., DuBois, D. W., King, J., and Shafer, D.: In situ observations of soil minerals and organic matter in the early phases of prescribed fires, Journal of Geophysical Research: Atmospheres, 117, https://doi.org/10.1029/2011JD017420, 2012.

Köhler, H.: The nucleus in and the growth of hygroscopic droplets, Transactions of the Faraday Society, 32, 1152-1161, 1936.

Kreidenweis, S., and Asa-Awuku, A.: Aerosol Hygroscopicity: Particle water content and its role in atmospheric processes, https://doi.org/10.1016/B978-0-08-095975-7.00418-6, 2014.

Kuang, Y., Zhao, C., Tao, J., Bian, Y., Ma, N., and Zhao, G.: A novel method for deriving the aerosol hygroscopicity parameter based only on measurements from a humidified nephelometer system, Atmospheric Chemistry and Physics, 17, 6651-6662, https://doi.org/10.5194/acp-17-6651-2017, 2017.

Kuang, Y., He, Y., Xu, W., Zhao, P., Cheng, Y., Zhao, G., Tao, J., Ma, N., Su, H., and Zhang, Y.: Distinct diurnal variation in organic aerosol hygroscopicity and its relationship with oxygenated organic aerosol, Atmospheric Chemistry and Physics, 20, 865-880, 2020.

Lacagnina, C., Hasekamp, O. P., Bian, H., Curci, G., Myhre, G., van Noije, T., Schulz, M., Skeie, R. B., Takemura, T., and Zhang, K.: Aerosol single-scattering albedo over the global oceans: Comparing PARASOL retrievals with AERONET, OMI, and AeroCom models estimates, Journal of Geophysical Research: Atmospheres, 120, 9814-9836, https://doi.org/10.1002/2015JD023501, 2015.

Lee, H.-H., Iraqui, O., Gu, Y., Yim, S. H.-L., Chulakadabba, A., Tonks, A. Y.-M., Yang, Z., and Wang, C.: Impacts of air pollutants from fire and non-fire emissions on the regional air quality in Southeast Asia, Atmos. Chem. Phys., 18, 6141-6156, https://doi.org/10.5194/acp-18-6141-2018, 2018.

Li, G., Bei, N., Cao, J., Huang, R., Wu, J., Feng, T., Wang, Y., Liu, S., Zhang, Q., and Tie, X.: A possible pathway for rapid growth of sulfate during haze days in China, Atmos. Chem. Phys., 17, 3301-3316, https://doi.org/10.5194/acp-17-3301-2017, 2017.

Liu, H., Zhao, C., Nekat, B., Ma, N., Wiedensohler, A., Van Pinxteren, D., Spindler, G., Müller, K., and Herrmann, H.: Aerosol hygroscopicity derived from size-segregated chemical composition and its parameterization in the North China Plain, Atmospheric Chemistry and Physics, 14, 2525-2539, https://doi.org/10.5194/acp-14-2525-2014, 2014.

Liu, J., and Li, Z.: Significant underestimation in the optically based estimation of the aerosol first indirect effect induced by the aerosol swelling effect, Geophysical Research Letters, 45, 5690-5699, https://doi.org/10.1029/2018GL077679, 2018.

Liu, X., Ma, P.-L., Wang, H., Tilmes, S., Singh, B., Easter, R., Ghan, S., and Rasch, P.: Description and evaluation of a new four-mode version of the Modal Aerosol Module (MAM4) within version 5.3 of the Community Atmosphere Model, Geoscientific Model Development, 9, 505-522, https://doi.org/10.5194/gmd-9-505-2016, 2016.

Lorenzo, G. R., Arellano, A. F., Cambaliza, M. O., Castro, C., Cruz, M. T., Di Girolamo, L., Gacal, G. F., Hilario, M. R. A., Lagrosas, N., Ong, H. J., Simpas, J. B., Uy, S. N., and Sorooshian, A.: An emerging aerosol climatology via remote sensing over Metro Manila, the Philippines, Atmospheric Chemistry and Physics, 23, 10579-10608, https://doi.org/10.5194/acp-23-10579-2023, 2023.

Malm, W. C., and Day, D. E.: Estimates of aerosol species scattering characteristics as a function of relative humidity, Atmospheric Environment, 35, 2845-2860, https://doi.org/10.1016/S1352-2310(01)00077-2, 2001.

1090   Mason, B., Wagner, N., Adler, G., Andrews, E., Brock, C., Gordon, T., Lack, D., Perring, A.,
1091   Richardson, M., and Schwarz, J.: An intercomparison of aerosol absorption measurements
1092   conducted during the SEAC4RS campaign, Aerosol Science and Technology, 52, 1012-1027,
1093   https://doi.org/10.1080/02786826.2018.1500012, 2018.
1094   Maudlin, L., Wang, Z., Jonsson, H., and Sorooshian, A.: Impact of wildfires on size-resolved
1095   aerosol composition at a coastal California site, Atmospheric Environment, 119, 59-68,
1096   https://doi.org/10.1016/j.atmosenv.2015.08.039, 2015.
1097   McNaughton, C. S., Clarke, A. D., Howell, S. G., Pinkerton, M., Anderson, B., Thornhill, L.,
1098   Hudgins, C., Winstead, E., Dibb, J. E., and Scheuer, E.: Results from the DC-8 Inlet
1099   Characterization Experiment (DICE): Airborne versus surface sampling of mineral dust and sea
1100   salt aerosols, Aerosol Science and Technology, 41, 136-159,
1101   https://doi.org/10.1080/02786820601118406, 2007.
1102   Miller, R. M., Rauber, R. M., Di Girolamo, L., Rilloraza, M., Fu, D., McFarquhar, G. M.,
1103   Nesbitt, S. W., Ziemba, L. D., Woods, S., and Thornhill, K. L.: Influence of natural and
1104   anthropogenic aerosols on cloud base droplet size distributions in clouds over the South China
1105   Sea and West Pacific, Atmospheric Chemistry and Physics, 23, 8959-8977,
1106   https://doi.org/10.5194/acp-23-8959-2023, 2023.
1107   Mochida, M., Kuwata, M., Miyakawa, T., Takegawa, N., Kawamura, K., and Kondo, Y.:
1108   Relationship between hygroscopicity and cloud condensation nuclei activity for urban aerosols in
1109   Tokyo, Journal of Geophysical Research: Atmospheres, 111,
1110   https://doi.org/10.1029/2005JD006980, 2006.
1111   Moosmüller, H., and Sorensen, C.: Small and large particle limits of single scattering albedo for
1112   homogeneous, spherical particles, J. Quant. Spectrosc. Ra., 204, 250-255,
1113   https://doi.org/10.1016/j.jqsrt.2017.09.029, 2018.
1114   Nakajima, T., Higurashi, A., Takeuchi, N., and Herman, J. R.: Satellite and ground-based study
1115   of optical properties of 1997 Indonesian forest fire aerosols, Geophysical Research Letters, 26,
1116   2421-2424, https://doi.org/10.1029/1999GL900208, 1999.
1117   NASA, E. D.: Fires in Kalimantan, Indonesia, in, Worldview Image of the Week, 2020.
1118   Oanh, N. K., Upadhyay, N., Zhuang, Y.-H., Hao, Z.-P., Murthy, D., Lestari, P., Villarin, J.,
1119   Chengchua, K., Co, H., and Dung, N.: Particulate air pollution in six Asian cities: Spatial and
1120   temporal distributions, and associated sources, Atmospheric environment, 40, 3367-3380,
1121   https://doi.org/10.1016/j.atmosenv.2006.01.050, 2006.
1122   Othman, M., Latif, M. T., Hamid, H. H. A., Uning, R., Khumsaeng, T., Phairuang, W., Daud, Z.,
1123   Idris, J., Sofwan, N. M., and Lung, S.-C. C.: Spatial–temporal variability and health impact of
1124   particulate matter during a 2019–2020 biomass burning event in Southeast Asia, Scientific
1125   Reports, 12, 7630, https://doi.org/10.1038/s41598-022-11409-z, 2022.
1126   Palmer, T. Y.: Large fire winds, gases and smoke, Atmospheric Environment (1967), 15, 2079-
1127   2090, https://doi.org/10.1016/0004-6981(81)90241-9, 1981.
1128   Pawar, P. V., Ghude, S. D., Jena, C., Móring, A., Sutton, M. A., Kulkarni, S., Lal, D. M.,
1129   Surendran, D., Van Damme, M., and Clarisse, L.: Analysis of atmospheric ammonia over South
1130   and East Asia based on the MOZART-4 model and its comparison with satellite and surface
1131   observations, Atmospheric Chemistry and Physics, 21, 6389-6409, https://doi.org/10.5194/acp-
1132   21-6389-2021, 2021.
1133   Petters, M., and Kreidenweis, S.: A single parameter representation of hygroscopic growth and
1134   cloud condensation nucleus activity, Atmospheric Chemistry and Physics, 7, 1961-1971,
1135   https://doi.org/10.5194/acp-7-1961-2007, 2007.

1136 Pfister, G. G., Eastham, S. D., Arellano, A. F., Aumont, B., Barsanti, K. C., Barth, M. C.,
1137 Conley, A., Davis, N. A., Emmons, L. K., and Fast, J. D.: The multi-scale infrastructure for
1138 chemistry and aerosols (MUSICA), Bulletin of the American Meteorological Society, 101,
1139 E1743-E1760, https://doi.org/10.1175/BAMS-D-19-0331.1, 2020.
1140 Pokhrel, R. P., Gordon, J., Fiddler, M. N., and Bililign, S.: Impact of combustion conditions on
1141 physical and morphological properties of biomass burning aerosol, Aerosol Science and
1142 Technology, 55, 80-91, https://doi.org/10.1080/02786826.2020.1822512, 2021.
1143 Pringle, K., Tost, H., Pozzer, A., Pöschl, U., and Lelieveld, J.: Global distribution of the effective
1144 aerosol hygroscopicity parameter for CCN activation, Atmospheric Chemistry and Physics, 10,
1145 5241-5255, https://doi.org/10.5194/acp-10-5241-2010, 2010.
1146 Quinn, P. K., Bates, T., Baynard, T., Clarke, A., Onasch, T., Wang, W., Rood, M., Andrews, E.,
1147 Allan, J., and Carrico, C.: Impact of particulate organic matter on the relative humidity
1148 dependence of light scattering: A simplified parameterization, Geophysical Research Letters, 32,
1149 https://doi.org/10.1029/2005GL024322, 2005.
1150 Radtke, J., Mauritsen, T., and Hohenegger, C.: Shallow cumulus cloud feedback in large eddy
1151 simulations–bridging the gap to storm-resolving models, Atmospheric Chemistry and Physics,
1152 21, 3275-3288, https://doi.org/10.5194/acp-21-3275-2021, 2021.
1153 Reid, J., Koppmann, R., Eck, T., and Eleuterio, D.: A review of biomass burning emissions part
1154 II: intensive physical properties of biomass burning particles, Atmos. Chem. Phys., 5, 799-825,
1155 https://doi.org/10.5194/acp-5-799-2005, 2005.
1156 Reid, J., Maring, H., Narisma, G., van den Heever, S., Di Girolamo, L., Ferrare, R., Holz, R.,
1157 Lawson, P., Mace, G., and Simpas, J.: The coupling between tropical meteorology, aerosol
1158 lifecycle, convection, and radiation, during the Cloud, Aerosol and Monsoon Processes
1159 Philippines Experiment (CAMP 2 Ex), B. Am. Meteorol. Soc., https://doi.org/10.1175/BAMS-
1160 D-21-0285.1, 2023.
1161 Reid, J. S., Hyer, E. J., Johnson, R. S., Holben, B. N., Yokelson, R. J., Zhang, J., Campbell, J. R.,
1162 Christopher, S. A., Di Girolamo, L., and Giglio, L.: Observing and understanding the Southeast
1163 Asian aerosol system by remote sensing: An initial review and analysis for the Seven Southeast
1164 Asian Studies (7SEAS) program, Atmos. Res., 122, 403-468,
1165 https://doi.org/10.1016/j.atmosres.2012.06.005, 2013.
1166 Robinson, M. S., Chavez, J., Velazquez, S., and Jayanty, R.: Chemical speciation of PM2. 5
1167 collected during prescribed fires of the Coconino National Forest near Flagstaff, Arizona, Journal
1168 of the Air & Waste Management Association, 54, 1112-1123,
1169 https://doi.org/10.1080/10473289.2004.10470985, 2004.
1170 Rolph, G., Stein, A., and Stunder, B.: Real-time environmental applications and display system:
1171 READY, Environ. Modell. Softw., 95, 210-228, https://doi.org/10.1016/j.envsoft.2017.06.025,
1172 2017.
1173 Ross, A. D., Holz, R. E., Quinn, G., Reid, J. S., Xian, P., Turk, F. J., and Posselt, D. J.: Exploring
1174 the first aerosol indirect effect over Southeast Asia using a 10-year collocated MODIS, CALIOP,
1175 and model dataset, Atmospheric Chemistry and Physics, 18, 12747-12764,
1176 https://doi.org/10.5194/acp-18-12747-2018, 2018.
1177 Saxena, P., Hildemann, L. M., McMurry, P. H., and Seinfeld, J. H.: Organics alter hygroscopic
1178 behavior of atmospheric particles, Journal of Geophysical Research: Atmospheres, 100, 18755-
1179 18770, https://doi.org/10.1029/95JD01835, 1995.
1180 Schlosser, J. S., Braun, R. A., Bradley, T., Dadashazar, H., MacDonald, A. B., Aldhaif, A. A.,
1181 Aghdam, M. A., Mardi, A. H., Xian, P., and Sorooshian, A.: Analysis of aerosol composition

data for western United States wildfires between 2005 and 2015: Dust emissions, chloride depletion, and most enhanced aerosol constituents, J. Geophys. Res.- Atmos., 122, 8951-8966, https://doi.org/10.1002/2017JD026547, 2017.

Schuster, G. L., Dubovik, O., and Holben, B. N.: Angstrom exponent and bimodal aerosol size distributions, J. Geophys. Res.- Atmos., 111, https://doi.org/10.1029/2005JD006328, 2006.

Schwantes, R. H., Lacey, F. G., Tilmes, S., Emmons, L. K., Lauritzen, P. H., Walters, S., Callaghan, P., Zarzycki, C. M., Barth, M. C., and Jo, D. S.: Evaluating the impact of chemical complexity and horizontal resolution on tropospheric ozone over the conterminous US with a global variable resolution chemistry model, Journal of Advances in Modeling Earth Systems, 14, e2021MS002889, https://doi.org/10.1029/2021MS002889, 2022.

Shi, J., Hong, J., Ma, N., Luo, Q., He, Y., Xu, H., Tan, H., Wang, Q., Tao, J., and Zhou, Y.: Measurement report: On the difference in aerosol hygroscopicity between high and low relative humidity conditions in the North China Plain, Atmospheric Chemistry and Physics, 22, 4599-4613, https://doi.org/10.5194/acp-22-4599-2022, 2022.

Shingler, T., Crosbie, E., Ortega, A., Shiraiwa, M., Zuend, A., Beyersdorf, A., Ziemba, L., Anderson, B., Thornhill, L., and Perring, A. E.: Airborne characterization of subsaturated aerosol hygroscopicity and dry refractive index from the surface to 6.5 km during the SEAC4RS campaign, Journal of Geophysical Research: Atmospheres, 121, 4188-4210, https://doi.org/10.1002/2015JD024498, 2016a.

Shingler, T., Sorooshian, A., Ortega, A., Crosbie, E., Wonaschütz, A., Perring, A. E., Beyersdorf, A., Ziemba, L., Jimenez, J. L., and Campuzano-Jost, P.: Ambient observations of hygroscopic growth factor and f (RH) below 1: Case studies from surface and airborne measurements, Journal of Geophysical Research: Atmospheres, 121, 13,661-613,677, https://doi.org/10.1002/2016JD025471, 2016b.

Smith, S. J., Aardenne, J. v., Klimont, Z., Andres, R. J., Volke, A., and Delgado Arias, S.: Anthropogenic sulfur dioxide emissions: 1850–2005, Atmos. Chem. Phys., 11, 1101-1116, https://doi.org/10.5194/acp-11-1101-2011, 2011.

Sorooshian, A., Shingler, T., Crosbie, E., Barth, M., Homeyer, C., Campuzano-Jost, P., Day, D., Jimenez, J., Thornhill, K., and Ziemba, L.: Contrasting aerosol refractive index and hygroscopicity in the inflow and outflow of deep convective storms: Analysis of airborne data from DC3, Journal of Geophysical Research: Atmospheres, 122, 4565-4577, https://doi.org/10.1002/2017JD026638, 2017.

Spill, G., Stier, P., Field, P. R., and Dagan, G.: Effects of aerosol in simulations of realistic shallow cumulus cloud fields in a large domain, Atmospheric Chemistry and Physics, 19, 13507-13517, https://doi.org/10.5194/acp-19-13507-2019, 2019.

Stein, A., Draxler, R. R., Rolph, G. D., Stunder, B. J., Cohen, M., and Ngan, F.: NOAA's HYSPLIT atmospheric transport and dispersion modeling system, B. Am. Meteorol. Soc., 96, 2059-2077, https://doi.org/10.1175/BAMS-D-14-00110.1, 2015.

Stockwell, C. E., Jayarathne, T., Cochrane, M. A., Ryan, K. C., Putra, E. I., Saharjo, B. H., Nurhayati, A. D., Albar, I., Blake, D. R., and Simpson, I. J.: Field measurements of trace gases and aerosols emitted by peat fires in Central Kalimantan, Indonesia, during the 2015 El Niño, Atmospheric Chemistry and Physics, 16, 11711-11732, https://doi.org/10.5194/acp-16-11711-2016, 2016.

Stokes, R., and Robinson, R.: Interactions in aqueous nonelectrolyte solutions. I. Solute-solvent equilibria, The Journal of Physical Chemistry, 70, 2126-2131, 1966.

1227 Swietlicki, E., Hansson, H.-C., Hämeri, K., Svenningsson, B., Massling, A., McFiggans, G.,
1228 McMurry, P. H., Petäjä, T., Tunved, P., and Gysel, M.: Hygroscopic properties of submicrometer
1229 atmospheric aerosol particles measured with H-TDMA instruments in various environments—a
1230 review, Tellus B: Chemical and Physical Meteorology, 60, 432-469,
1231 https://doi.org/10.1111/j.1600-0889.2008.00350.x, 2008.
1232 Thalman, R., de Sá, S. S., Palm, B. B., Barbosa, H. M., Pöhlker, M. L., Alexander, M. L., Brito,
1233 J., Carbone, S., Castillo, P., and Day, D. A.: CCN activity and organic hygroscopicity of aerosols
1234 downwind of an urban region in central Amazonia: seasonal and diel variations and impact of
1235 anthropogenic emissions, Atmospheric Chemistry and Physics, 17, 11779-11801,
1236 https://doi.org/10.5194/acp-17-11779-2017, 2017.
1237 Tilmes, S., Mills, M. J., Zhu, Y., Bardeen, C. G., Vitt, F., Yu, P., Fillmore, D., Liu, X., Toon, B.,
1238 and Deshler, T.: Description and performance of a sectional aerosol microphysical model in the
1239 Community Earth System Model (CESM2), Geoscientific Model Development, 16, 6087-6125,
1240 https://doi.org/10.5194/gmd-16-6087-2023, 2023.
1241 Titos, G., Burgos, M. A., Zieger, P., Alados-Arboledas, L., Baltensperger, U., Jefferson, A.,
1242 Sherman, J., Weingartner, E., Henzing, B., and Luoma, K.: A global study of hygroscopicity-
1243 driven light-scattering enhancement in the context of other in situ aerosol optical properties,
1244 Atmospheric Chemistry and Physics, 21, 13031-13050, https://doi.org/10.5194/acp-21-13031-
1245 2021, 2021.
1246 Tsay, S.-C., Hsu, N. C., Lau, W. K.-M., Li, C., Gabriel, P. M., Ji, Q., Holben, B. N., Welton, E.
1247 J., Nguyen, A. X., and Janjai, S.: From BASE-ASIA toward 7-SEAS: A satellite-surface
1248 perspective of boreal spring biomass-burning aerosols and clouds in Southeast Asia,
1249 Atmospheric environment, 78, 20-34, https://doi.org/10.1016/j.atmosenv.2012.12.013, 2013.
1250 van Diedenhoven, B., Hasekamp, O. P., Cairns, B., Schuster, G. L., Stamnes, S., Shook, M., and
1251 Ziemba, L.: Remote sensing of aerosol water fraction, dry size distribution and soluble fraction
1252 using multi-angle, multi-spectral polarimetry, Atmospheric Measurement Techniques, 15, 7411-
1253 7434, https://doi.org/10.5194/amt-15-7411-2022, 2022.
1254 Virkkula, A.: Correction of the calibration of the 3-wavelength Particle Soot Absorption
1255 Photometer (3λ PSAP), Aerosol Science and Technology, 44, 706-712,
1256 https://doi.org/10.1080/02786826.2010.482110, 2010.
1257 Waggoner, A., Weiss, R., and Larson, T.: In-situ, rapid response measurement of H2SO4/(NH4)
1258 2SO4 aerosols in urban Houston: A comparison with rural Virginia, Atmospheric Environment
1259 (1967), 17, 1723-1731, https://doi.org/10.1016/0004-6981(83)90179-8, 1983.
1260 Wang, X., Ye, X., Chen, H., Chen, J., Yang, X., and Gross, D. S.: Online hygroscopicity and
1261 chemical measurement of urban aerosol in Shanghai, China, Atmospheric Environment, 95, 318-
1262 326, https://doi.org/10.1016/j.atmosenv.2014.06.051, 2014.
1263 Wang, Y., Li, Z., Zhang, Y., Du, W., Zhang, F., Tan, H., Xu, H., Fan, T., Jin, X., and Fan, X.:
1264 Characterization of aerosol hygroscopicity, mixing state, and CCN activity at a suburban site in
1265 the central North China Plain, Atmospheric Chemistry and Physics, 18, 11739-11752,
1266 https://doi.org/10.5194/acp-18-11739-2018, 2018.
1267 Wu, Z., Zheng, J., Shang, D., Du, Z., Wu, Y., Zeng, L., Wiedensohler, A., and Hu, M.: Particle
1268 hygroscopicity and its link to chemical composition in the urban atmosphere of Beijing, China,
1269 during summertime, Atmospheric Chemistry and Physics, 16, 1123-1138,
1270 https://doi.org/10.5194/acp-16-1123-2016, 2016.
1271 Xu, W., Ovadnevaite, J., Fossum, K. N., Lin, C., Huang, R.-J., O'Dowd, C., and Ceburnis, D.:
1272 Aerosol hygroscopicity and its link to chemical composition in the coastal atmosphere of Mace

Head: marine and continental air masses, Atmospheric Chemistry and Physics, 20, 3777-3791, https://doi.org/10.5194/acp-20-3777-2020, 2020.

Yang, Q., Easter, R. C., Campuzano-Jost, P., Jimenez, J. L., Fast, J. D., Ghan, S. J., Wang, H., Berg, L. K., Barth, M. C., and Liu, Y.: Aerosol transport and wet scavenging in deep convective clouds: A case study and model evaluation using a multiple passive tracer analysis approach, Journal of Geophysical Research: Atmospheres, 120, 8448-8468, https://doi.org/10.1002/2015JD023647, 2015.

Zhang, F., Wang, Y., Peng, J., Ren, J., Collins, D., Zhang, R., Sun, Y., Yang, X., and Li, Z.: Uncertainty in predicting CCN activity of aged and primary aerosols, Journal of Geophysical Research: Atmospheres, 122, 11,723-711,736, https://doi.org/10.1002/2017JD027058, 2017.

Zhang, L., Sun, J., Shen, X., Zhang, Y., Che, H., Ma, Q., Zhang, Y., Zhang, X., and Ogren, J.: Observations of relative humidity effects on aerosol light scattering in the Yangtze River Delta of China, Atmospheric Chemistry and Physics, 15, 8439-8454, https://doi.org/10.5194/acp-15-8439-2015, 2015.

Zhao, G., Zhao, C., Kuang, Y., Bian, Y., Tao, J., Shen, C., and Yu, Y.: Calculating the aerosol asymmetry factor based on measurements from the humidified nephelometer system, Atmos. Chem. Phys., 18, 9049-9060, https://doi.org/10.5194/acp-18-9049-2018, 2018.

Zieger, P., Fierz-Schmidhauser, R., Gysel, M., Ström, J., Henne, S., Yttri, K. E., Baltensperger, U., and Weingartner, E.: Effects of relative humidity on aerosol light scattering in the Arctic, Atmospheric Chemistry and Physics, 10, 3875-3890, https://doi.org/10.5194/acp-10-3875-2010, 2010.

Zieger, P., Fierz-Schmidhauser, R., Weingartner, E., and Baltensperger, U.: Effects of relative humidity on aerosol light scattering: results from different European sites, Atmospheric Chemistry and Physics, 13, 10609-10631, https://doi.org/10.5194/acp-13-10609-2013, 2013.

Zieger, P., Fierz-Schmidhauser, R., Poulain, L., Müller, T., Birmili, W., Spindler, G., Wiedensohler, A., Baltensperger, U., and Weingartner, E.: Influence of water uptake on the aerosol particle light scattering coefficients of the Central European aerosol, Tellus B: Chemical and Physical Meteorology, 66, 22716, https://doi.org/10.3402/tellusb.v66.22716, 2014.

Ziemba, L. D., Lee Thornhill, K., Ferrare, R., Barrick, J., Beyersdorf, A. J., Chen, G., Crumeyrolle, S. N., Hair, J., Hostetler, C., and Hudgins, C.: Airborne observations of aerosol extinction by in situ and remote-sensing techniques: Evaluation of particle hygroscopicity, Geophysical Research Letters, 40, 417-422, https://doi.org/10.1029/2012GL054428, 2013.